



저작자표시-비영리-동일조건변경허락 2.0 대한민국

이용자는 아래의 조건을 따르는 경우에 한하여 자유롭게

- 이 저작물을 복제, 배포, 전송, 전시, 공연 및 방송할 수 있습니다.
- 이차적 저작물을 작성할 수 있습니다.

다음과 같은 조건을 따라야 합니다:



저작자표시. 귀하는 원저작자를 표시하여야 합니다.



비영리. 귀하는 이 저작물을 영리 목적으로 이용할 수 없습니다.



동일조건변경허락. 귀하가 이 저작물을 개작, 변형 또는 가공했을 경우에는, 이 저작물과 동일한 이용허락조건하에서만 배포할 수 있습니다.

- 귀하는, 이 저작물의 재이용이나 배포의 경우, 이 저작물에 적용된 이용허락조건을 명확하게 나타내어야 합니다.
- 저작권자로부터 별도의 허가를 받으면 이러한 조건들은 적용되지 않습니다.

저작권법에 따른 이용자의 권리는 위의 내용에 의하여 영향을 받지 않습니다.

이것은 [이용허락규약\(Legal Code\)](#)을 이해하기 쉽게 요약한 것입니다.

[Disclaimer](#)

Ph.D. DISSERTATION

**Deposition and Characterization of Molybdenum-
based Metal Oxides by Reactive DC Magnetron
Sputtering for Application of
Transparent Conducting Electrode**

by

Myeong Sook Oh

August 2012

Department of Materials Science and Engineering

College of Engineering

Seoul National University

**Deposition and Characterization of Molybdenum-based
Metal Oxides by Reactive DC Magnetron Sputtering for
Application of Transparent Conducting Electrode**

Advisor : Prof. Hyeong Joon Kim

**By
Myeong Sook Oh**

**A thesis submitted to the Graduate Faculty of Seoul National
University in partial fulfillment of the requirements for the
Degree of Doctor of Philosophy
Department of Materials Science and Engineering**

June 2012

**Approved
by**

Chairman of Advisory Committee : Cheol Seong Hwang

Vice-chairman of Advisory Committee : Hyeong Joon Kim

Advisory Committee : Seong Hyeon Hong

Advisory Committee : Myung Soo Huh

Advisory Committee : Jae Kyeong Jeong

Abstract

Nowadays transparent conducting oxides (TCO) are of interest because of a strong demand in the display industry. Especially TCO films which can replace ITO film attract a great attention due to the scarcity and high price of Indium. Molybdenum oxide (MoO_x) is one of candidate oxides to replace ITO film because its electrical and optical properties can be changed depending on oxygen vacancy concentration and non-stoichiometry. Meanwhile, for decades p-type TCO materials as well as n-type TCOs have been also developed to produce transparent electronics based on p-n junction. However, compared with the n-type TCOs, p-type TCOs have relatively lower conductivities, of the order of 1 S/cm, and lower transmittance, < 80 %. Therefore, research for good quality p-type TCOs is one of major goals for material scientists.

This dissertation presents the preparation and characterization of molybdenum-based binary and ternary oxide films for applications as a transparent conducting electrode. Two types of TCO, molybdenum oxide (MoO_x) and indium doped molybdenum oxide (In:MoO_x), have been deposited by dc magnetron reactive sputtering, followed by post-deposition annealing (PDA) in argon ambient for crystallization.

1st, the TCO properties of MoO_x films formed by the ultra-low pressure sputtering (ULPS) method were demonstrated. A very low resistivity was

obtained at O/Mo atomic ratio ≈ 2.85 (high O_2 content), in which only metallic crystal phases, such as MoO_2 , Magnéli, and β - MoO_3 , without any insulating orthorhombic MoO_3 phase, were detected in the XRD data. This means that the MoO_x films formed by ULPS method can possess better transparent and conductive properties than those formed at higher sputtering pressures. The maximum value of the transmittance was about 73 % within the 400-500 nm wavelength range and the resistivity was $1.05 \times 10^{-3} \Omega \cdot cm$. This performance was superior to the previously reported PLD MoO_x .

2nd, MoO_x ($x \approx 3$) films were annealed at the temperatures from 250 °C to 450 °C in order to investigate material properties according to formed MoO_x phases. The films annealed below 350 °C were crystallized in monoclinic MoO_3 (β -phase), and those annealed at 400 °C were crystallized in orthorhombic MoO_3 (α -phase). Meanwhile, in the MoO_3 film annealed at 450 °C, only γ - Mo_4O_{11} (Magnéli) phase which is known to be metallic was detected by XRD without orthorhombic α - MoO_3 phase. It was verified that sub-stoichiometric Magnéli MoO_{3-x} (γ - Mo_4O_{11}) phase could be formed through 450 °C PDA due to the sublimation of MoO_3 species and a little loss of oxygen ions in initial film. The resistivity value of 400 °C and 450 °C PDA MoO_x films was obtained to $5.7 \times 10^{-4} \Omega \cdot cm$ and $1.5 \times 10^{-3} \Omega \cdot cm$, respectively. The transmittance of them was 76 % and 50 % at the wavelength of 550nm, respectively.

Finally, indium doped MoO_x ($In:MoO_x$) films were prepared with MoIn

compound target by dc reactive magnetron sputtering method. By Hall measuring In:MoO_x films were identified as p-type oxide. From XRD analysis of In:MoO_x films annealed in the range from 250 °C to 450 °C, it was revealed that indium dopants acted as an inhibitor to crystallization in In:MoO_x films. Also the electrical and optical properties of In:MoO_x films with different indium content were investigated. As the indium content increased up to 3.1 at %, the resistivity gradually decreased and the minimum resistivity was achieved in $7.05 \times 10^{-4} \Omega\cdot\text{cm}$. The transmittance and optical band gap were increased with increasing indium content and those for 3.1 at % In-doped film was achieved about 80 % and 3.37 eV, respectively.

Keywords : Transparent Conducting Oxide (TCO), Molybdenum Oxide (MoO_x), Indium doped Molybdenum Oxide (In:MoO_x), Utralow-pressure Sputtering Method (ULPS), DC Magnetron Reactive Sputtering, Compressive Stress-induced Crystallization, P-type TCO

Student Number : 2006-30190

Myeong Sook Oh

Table of Contents

Abstract	i
Table of Contents	iv
List of Tables	vii
List of Figures	viii
List of Abbreviations	xiii
I. Introduction	1
1.1. Overview	1
1.2. Outline of dissertation	6
II. Literature Review	7
2.1. Basic material properties of Molybdenum oxides (MoO_x)	7
2.1.1. Band structure and electronic properties of MoO_x	8
2.1.2. Molybdenum trioxide (MoO_3)	11
2.1.3. Molybdenum dioxide (MoO_2)	15
2.1.4. Magnéli and related phases	17
2.1.5. Hydrogen molybdenum bronzes (H_xMoO_3)	20
2.2. Review on molybdenum-contained ternary oxides	22
2.3. Ultralow-pressure Sputtering Method	25
2.4. Figure of merit	28

III. Experiments and Analysis	32
3.1. Sputter and furnace system for film preparation	32
3.2. Resistivity and Hall effect	35
3.3. Stress measurement	40
3.4. Extraction of optical band-gap energy	43
3.5. Analysis Methods	44
3.6. Deposition of MoO _x Films (chap. 4.1- 4.2).....	46
3.7. Deposition of In:MoO _x Films (chap. 4.3).....	50
IV. Results and Discussions	53
4.1. Effects of sputtering pressure on the TCO properties of MoO _x films.....	53
4.1.1. Deposition characteristics	53
4.1.2. Structural properties	56
4.1.3. Electrical and Optical properties.....	64
4.1.4. Effects of residual stresses of MoO _x films on crystallization	71
4.1.5. Summary	74
4.2. Effects of post-deposition annealing (PDA) temperature on the structural, electrical and optical properties of MoO _x (x≈3) films	76
4.2.1. Structural evolution according to PDA temperature	76
4.2.2. Sublimation behavior and chemical bonding changes	80
4.2.3. Crystalline shapes and surface morphology	89

4.2.4. Electrical and optical properties -----	94
4.2.5. Summary -----	99
4.3. Preparation and TCO properties of In:MoO _x films -----	101
4.3.1. Indium doping effect on crystallization behavior -----	101
4.3.2. Influence of indium doping concentration on electrical and optical properties -----	103
4.3.3. Summary -----	107
V. Conclusions -----	108
VI. Bibliography -----	110
List of publications -----	121
Abstract (in Korean) -----	129
Acknowledgement (감사의 글) -----	132

List of Tables

Table 1-1. Electrical and optical properties of some TCOs.

Table 2-1. Crystal data of molybdenum oxides.

Table 2-2. Electrical and optical data of In:MoO₃ nanowire and thin films.

Table 2-3. Comparison of values of figure of merit ϕ_{TC} for different films.

Table 3-1. Detailed deposition and PDA conditions for MoO_x films.

Table 3-2. Detailed deposition and PDA conditions for In:MoO_x films.

Table 4-1. Comparison of optical and electrical properties of MoO_x films deposited by reactive sputtering and pulsed laser deposition.

Table 4-2. Area fraction of Mo⁶⁺, Mo⁵⁺ and oxygen related peaks in MoO_x films produced at PDA temperatures of 350 °C, 400 °C, and 450 °C.

Table 4-3. Comparison of surface roughness of the MoO_x films annealed in different temperature.

Table 4-4. Comparison of the transparent conductive oxide (TCO) performance of ITO and MoO_x films.

List of Figures

Fig. 1.1. Reported resistivity of impurity-doped binary compound TCO films, 1972-present: impurity-doped SnO₂ (□), In₂O₃ (Δ) and ZnO (•).

Fig. 2.1. Schematic Band Structure applicable to the bronzes.

Fig. 2.2. An idealized representation of the structure of (a) α-MoO₃ and (b) β - MoO₃.

Fig. 2.3. Valence and conduction band structure for (a) α-MoO₃ and (b) β - MoO₃ in a typical orthorhombic reciprocal space path, all the high-symmetry positions of the first Brillouin zone. All energies ε(k) are taken with respect to the fermi energy.

Fig. 2.4. (a) The structure of MoO₂ and (b) the coordination about the molybdenum atom showing the short Mo-Mo bonding.

Fig. 2.5. Molybdenum oxides and their formation temperatures.

Fig. 2.6. Band structures and electronic densities of state for several hydrogen molybdenum bronzes, H_{0.25}MoO₃, H_{0.5}MoO₃, HMoO₃, and H_{1.5}MoO₃. The energies are relative to the Fermi level.

Fig. 2.7. Measured XRR data and HRTEM images for the SnO_x films deposited by CSP and ULPS. Each inset shows an enlarged graph of the XRR spectra and the diffraction patterns for the SnO_x films: (a) The measured XRR data and (b) the HRTEM images.

Fig. 3.1. The sputtering system with 5-angle cluster module; (a) a total image of sputtering equipments and (b) enhanced magnetic field structure

of cathode (right) compared to the general type (left)..

Fig. 3.2. (a) Front-view of furnace system (b) schematic diagram of the apparatus for post-deposition annealing.

Fig. 3.3. Basic setup to measure carrier concentration using the Hall effect.

Fig. 3.4. Sequence of events leading to (a) residual tensile stress in film; (b) residual compressive stress in film.

Fig. 3.5. Schematic diagram for bending of MoO_x(100 nm)/Si(100 μm) stacks.

Fig. 3.6. Photograph for MoIn metallic target: One indium chip was attached on Mo target.

Fig. 4.1. Deposition rate of MoO_x films as a function of the O₂ content (%) in the sputtering gas (Ar + O₂) at the sputtering pressures of 6.7×10^{-1} , 1.3×10^{-1} , and 6.7×10^{-2} Pa.

Fig. 4.2. XRD patterns of as-deposited and PDA MoO_x films (at 450 °C for 8 h in Ar ambient) in the sputtering pressure of (a) and (d) 6.7×10^{-1} Pa, (b) and (e) 1.3×10^{-1} Pa, and (c) and (f) 6.7×10^{-2} Pa, respectively, at the O₂ contents of 10, 20, 30, and 40 %.

Fig. 4.3. O/Mo ratio of the PDA MoO_x films, which was analyzed by RBS, as a function of the sputtering pressure at O₂ contents of 10 %, 20 %, 30 %, and 40 %.

Fig. 4.4. Measured XRR data for (a) O/Mo \approx 2.0 and (b) O/Mo \approx 2.85, and (c) the variation of density of as-deposited MoO_x films with O/Mo \approx 2.0 and 2.85 as a function of sputtering pressure.

Fig. 4.5. Stress in as-deposited MoO_x films for O/Mo ≈ 2.0 and 2.85 as a function of sputtering pressure.

Fig. 4.6. Dependence of the electrical resistivity (ρ) on O₂ content in the sputtering pressures of 6.7×10^{-1} , 1.3×10^{-1} , and 6.7×10^{-2} Pa; closed squares denote ρ values of as-deposited MoO_x films and open squares denote those of PDA MoO_x films.

Fig. 4.7. Variation of the electrical resistivity (ρ), Hall mobility (μ), and carrier concentration (n) of PDA MoO_x films (450 °C, 8 h, Ar) with the O₂ content in sputtering ambient. The sputtering pressure was 6.7×10^{-2} Pa.

Fig. 4.8. Optical transmittance as a function of wavelength: (a) PDA-ULPS MoO_x films (sputtering pressure 6.7×10^{-2} Pa) with various O₂ contents and (b) PDA MoO_x films deposited in various sputtering pressures (The ratio of O/Mo is about 2.85).

Fig. 4.9. XRD patterns of MoO_x films annealed at different stress conditions for O/Mo ≈ (a) 2.0, (b) 2.85, and (c) 3.0.

Fig. 4.10. XRD spectra for MoO_x ($x \approx 3$) films with different post-deposition annealing temperature.

Fig. 4.11. Cross-sectional high-resolution TEM images for the PDA temperatures of (a) 350 °C, (b) 400 °C, and (c) 450 °C.

Fig. 4.12. The variation in thickness of MoO_x ($x \approx 3$) films according to post-deposition annealing temperature measured by ellipsometry.

Fig. 4.13. AES depth profiles of MoO_x/SiO₂ (100nm)/Si stacks. The dotted lines (1) and (2) indicate the interface between MoO_x and SiO₂.

Fig. 4.14. The cross-sectional SEM images of MoO_x/SiO₂(100nm)/Si stacks as a function of post-deposition annealing condition; (a) 350 °C-2hrs, (b) 400 °C-2hrs, (c) 450 °C-2hrs, and (d) 450 °C-8hrs. The thickness of top MoO_x film decreases in proportion to increase of PDA temperature and during-time.

Fig. 4.15. (a) Mo 3*d* and (b) O 1*s* XPS spectra of the MoO_x films annealed at temperature of 350 °C, 400 °C, and 450 °C.

Fig. 4.16. The Nomarski (or DIC) optical surface micrographs of the MoO_x films for magnification of × 1000. (a) as-deposited, (b) 250 °C, (c) 300 °C, (d) 350 °C, (e) 400 °C, and (f) 450 °C annealed films. The inset figure is for magnification of × 200.

Fig. 4.17. The AFM images of each film: (a) as-deposited, (b) 250 °C, (c) 300 °C, (d) 350 °C, (e) 400 °C, and (f) 450 °C annealed films.

Fig. 4.18. Variation of the electrical resistivity (ρ), Hall mobility (μ), and carrier concentration (n) of MoO_x films annealed at the temperature of 350 °C, 400 °C, and 450 °C.

Fig. 4.19. (a) optical transmittance as a function of wavelength and (b) optical band gap energies for ITO and MoO_x films.

Fig. 4.20. XRD spectra for In:MoO_x (In 2.1 wt %) films with different post-deposition annealing temperature.

Fig. 4.21. Variation of the electrical resistivity, Hall mobility, and carrier concentration of In:MoO_x films annealed at the temperature of 400 °C for 2 hours, as a function of indium doping concentration.

Fig. 4.22. Optical transmittance as a function of wavelength and (b) optical band gap energies for In: MoO_x films with different indium doping concentration.

List of Abbreviations

AES	Auger Electron Spectroscopy
AFM	Atomic Force Microscope
CSP	Conventional Sputtering Pressure
EDS	Energy Dispersive Spectroscopy
FESEM	Field Emission Scanning Electron Microscope
FOM	Figure of Merit
FPD	Flat Panel Display
HRTEM	High Resolution Transmission Electron Microscope
DIC	Differential Interference Contrast
LED	Light-Emitting Diode
PDA	Post Deposition Annealing
PLD	Pulsed Laser Deposition
PV	Photo-Voltaic
TCO	Transparent Conduction Oxide
TEM	Transmission Electron Microscope
ULPS	Ultra-low Pressure Sputtering
XPS	X-ray Photoelectron Spectroscopy
XRD	X-ray Diffraction
XRF	X-ray Fluorescence spectrometer
XRR	X-Ray Reflectivity

I. Introduction

1.1. Overview

Transparent and conductive oxides (TCOs) are materials that possess both high electrical conductivity ($\geq 10^3 \text{ S}\cdot\text{cm}^{-1}$) and high optical transparency ($\geq 80\%$) in the visible range of the electromagnetic spectrum [1]. They usually have a carrier concentration (N) of the order of 10^{20} cm^{-3} or higher and an optical band-gap (E_g) above approximately 3.0 eV: i.e., degenerated n-type or p-type semiconductors [2]. This remarkable combination of conductivity and transparency is usually impossible in intrinsic stoichiometric oxides. However, it can be achieved by producing them with a non-stoichiometric composition or by introducing well-chosen dopants. Transparent and conductive layers of some metallic oxides, such as cadmium oxide (CdO), tin oxide (SnO_2), indium oxide (In_2O_3), zinc oxide (ZnO), have been known for a long time. CdO thin films were first reported by Badeker who prepared these films by thermal oxidation of sputtered films of cadmium [3]. Later, binary or ternary oxides, containing one or two metallic elements, consistently have been studied. The optical and electrical properties of the principal n-type TCOs are listed in Table 1-1 [1], and the change in minimum resistivity of impurity-doped binary compound TCO films reported in recent years is shown in Fig. 1.1 [2]. Among them, tin doped In_2O_3 (ITO), Al doped ZnO (AZO), and

fluorine or antimony doped SnO₂ (FTO and ATO) are the most utilized TCO thin films in modern technology. In particular, ITO, which is composed of typically 90% In₂O₃ and 10% SnO₂ by weight, is used extensively. ITO is a heavily-doped n-type semiconductor with a large optical band gap greater than 3.75 eV. These films have $N \approx 10^{21} \text{ cm}^{-3}$ and mobility (μ) lies in the range of $15 \sim 40 \text{ cm}^2 \cdot \text{V}^{-1} \cdot \text{s}^{-1}$ leading to resistivity (ρ) in the range from 7×10^{-5} to $5 \times 10^{-4} \text{ } \Omega \cdot \text{cm}$. The optical transmission in the visible and near-IR regions is high, the absorption is typically about 2% [4]. Despite these excellent transparent and conductive properties, there are several obstacles for the use of ITO: (1) the scarcity and high price of indium, (2) poor chemical stability in hydrogen atmospheres, and (3) poor diffusion barrier characteristics of ITO films [5]. The alternative TCO materials have been developed and AZO is now recognized as the most promising alternative. But various problems associated with AZO, such as non-stability in acidic solutions and severe degradation due to moisture, were also found [6]. Consequently, finding for new TCO materials should be continued, because electron work function, abrasion resistance, and compatibility with substrate and other components of a given device should be also considered together with optical and electrical properties, as appropriate for the application.

With the advent of flat panel displays (FPDs), flexible displays, and smart devices, the demand for TCOs has sharply increased [7]. The actual and potential applications of TCO films are transparent electrodes for light

emitting diodes (LEDs) and photovoltaic (PV) cells, transparent heating elements for automobile and aircraft windows, gas sensors, and anti-reflecting coatings [8-13].

Furthermore, a development of available p-type TCOs could widen the range of applications by forming transparent p-n junction, which is an essential structure in a wide variety of semiconductor devices. Fabricating undoped or doped p-type TCOs was found to be more difficult than the n-type. The first p-type TCO was made from CuAlO_2 by Kawazoe in 1997 [14]. After that, Cu-based p-type TCOs were actively investigated, of which the representative materials are CuGaO_2 , and SrCu_2O_2 , N or P doped ZnO, SnO, NiO and so on [15-20]. However, compared with the n-type TCOs, these TCOs have relatively lower conductivities, of the order of 1 S/cm, and lower transmittance, < 80 % [21-23]. Therefore, research for good quality p-type TCOs is a major goal for material scientists.

Table 1-1. Electrical and optical properties of some TCOs [1].

TCO	Deposition method	Carrier concentration (cm^{-3})	Mobility ($\text{cm}^2 \cdot \text{V}^{-1} \cdot \text{s}^{-1}$)	Resistivity ($\Omega \cdot \text{cm}$)	Average transmission (%)
TO	CVD	9×10^{18}	10	7×10^{-2}	90 ~ 95
ATO	CVD	1.2×10^{20}	23	2×10^{-3}	85 ~ 91
FTO	Spray pyrolysis	5×10^{20}	23	5×10^{-4}	85
IO	Evaporation	4.7×10^{20}	74	1.8×10^{-4}	90
	Evaporation	3.8×10^{20}	43	3.7×10^{-4}	80 ~ 90
ITO	R.f. sputter	6×10^{20}	35	3×10^{-4}	90
	Magnetron sputter	$\approx 10^{21}$	10	4×10^{-4}	85
ZO	Magnetron sputter	2×10^{20}	16	2×10^{-3}	90
AZO	Spray pyrolysis	4×10^{19}	20	7×10^{-3}	80 ~ 85
IZO	Spray pyrolysis	4×10^{20}	15	8×10^{-4}	90
CTO	R.f. sputter	2×10^{21}	30	1.7×10^{-4}	85

※ TO: tin oxide, ATO: antimony doped tin oxide, FTO: fluorine doped tin oxide, IO: indium oxide, ITO: tin doped indium oxide, AZO: aluminum doped zinc oxide, IZO: indium doped zinc oxide, CTO: cadmium stannate doped zinc oxide.

※ Transmission is average in the range of 400nm to 700nm

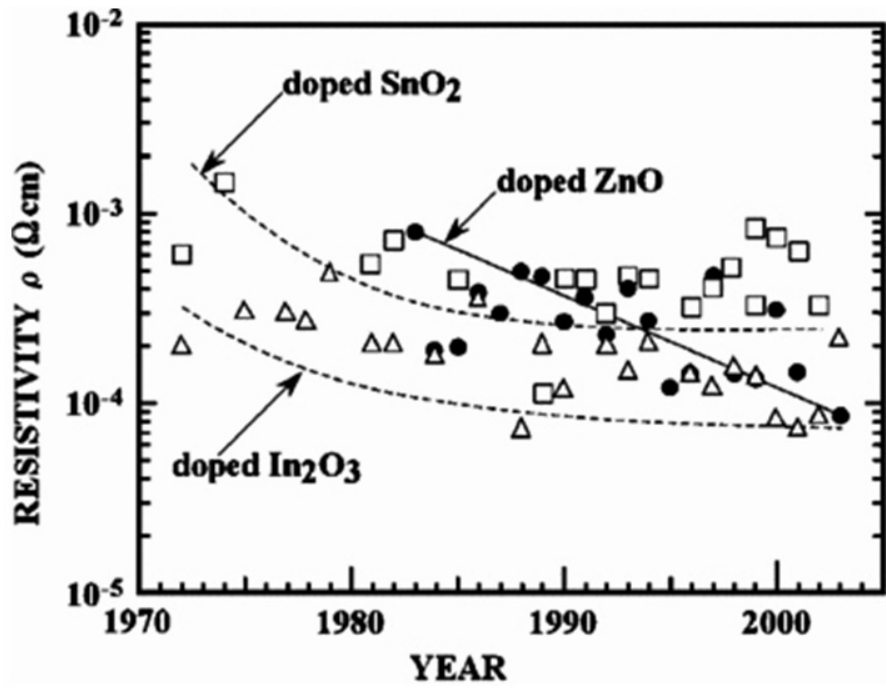


Fig. 1.1. Reported resistivity of impurity-doped binary compound TCO films, 1972-present: impurity-doped SnO_2 (\square), In_2O_3 (Δ) and ZnO (\bullet) [2].

1.2. Outline of dissertation

This dissertation discusses TCO properties of molybdenum oxides and indium-doped molybdenum oxides deposited by dc reactive magnetron sputtering, and effects of deposition conditions and post-deposition annealing process on them.

The dissertation consists of five chapters. The first chapter will give an overview of the subject of transparent conducting oxide (TCO) thin films and an outline of the dissertation. The second chapter provides primarily the basic material properties of diverse MoO_x phases, ternary molybdenum oxides and ULPS. The third chapter explained the experimental and analysis and MoIn compound target production method, including the basic comprehension of Hall measurement, stress measurement, optical band gap extraction. The fourth chapter presents TCO properties of binary MoO_x films and ternary indium doped MoO_x (In:MoO_x) films in accordance with sputtering parameters and post-deposition annealing condition. In particular, the effect of stress on crystallization of MoO_x films and p-type character of In:MoO_x films are appreciable. The fifth chapter presents conclusions.

II. Literature Review

2.1. Basic material properties of molybdenum oxides (MoO_x) [24,25]

The oxides of molybdenum are noted for their rich and diverse chemistries and structure. The binary oxides, for example, include not only the important dioxide (MoO_2) and trioxide (MoO_3), but also a remarkable homologous series of intermediate phase of general formula $\text{Mo}_n\text{O}_{3n-m}$ (e.g. $n=8,9;m=1$). The ternary oxides are even more versatile with molybdenum in oxidation states as low as 2.5. These molybdenum oxide materials have been used in a wide variety of industrial applications, such as catalysts, sensors, batteries and so on.

The wide ranging nature of molybdenum oxide chemistry stems in part from the ability of the metal to exist in a number of oxidation states. Particularly important is the delicate balance between these different states; a feature illustrated by the apparent coexistence of Mo^{6+} , Mo^{5+} , and Mo^{4+} in epitaxially grown MoO_x films by Bhosle et al. [26]. Another important facet of molybdenum chemistry is the adaptability of Mo^{6+} , which, unlike Cr^{6+} , W^{6+} , is found in a number of different coordination geometries. Hence, there is a diversity in the structure and bonding of molybdenum oxide materials that is not found with most other elements [27].

2.1.1. Band structure and electronic properties of MoO_x [25]

Figure 2.1 shows a schematic diagram of the band structure of the common bonding pattern in the bronzes (A_xMO_3) and the parent oxide (e.g. MoO_3 , WO_3 , ReO_3) [28-30]. For a discrete MO_6 unit (in the 4d transition metal series) $5p$, $5s$, and $4d(e_g)$ orbitals overlap with six sp hybrid orbitals of the oxygen atom to give a set of six bonding σ and six antibonding σ^* molecular orbitals. In the extended lattice, the discrete energy levels arising from this structure unit will broaden into bands. The metal $4d(t_{2g})$ orbitals can overlap with three of the surrounding oxygen $p\pi$ orbitals per octahedron to form bonding π and antibonding π^* bands. The σ and π bands are filled and constitute the valence bands separated by a large energy gap ($3 \sim 4$ eV) from the π^* conduction band. This band is empty in WO_3 and MoO_3 , so these materials are insulators, but is partially filled in ReO_3 , which is a metal.

In the bronzes, $\text{A}_x\text{M}_y\text{O}_z$, the A cations transfer their valence electrons to the usually empty π^* -levels with strong d -character. The extent of delocalization of the d electrons characterizes the transport and optical properties of any specific bronze. The orbitals of the A cation do not contribute to the formation of these levels, as is confirmed by several reports [31,32]. In the molybdenum bronzes the $4d$ orbitals have a radial extension intermediate between the $3d$ (localized) and $5d$ (delocalized) states and these materials show complex electronic behavior; the blue, $\text{A}_{0.3}\text{MoO}_3$ and purple, $\text{A}_{0.9}\text{Mo}_6\text{O}_{17}$ bronzes are

metallic at ambient temperature, while the red $A_{0.33}MoO_3$ bronzes are semiconducting.

The bronzes, $Na_{0.90-0.97}MoO_3$, $K_{0.89-0.93}MoO_3$, $K_{0.5}MoO_3$ and $Ru_{0.27}MoO_3$, have not been studied extensively, but are known to be metallic [33,34]. A relatively new class of compounds are the hydrogen molybdenum bronzes H_xMoO_3 ($0 < x \leq 2.0$) and the structure of each is closely related to that of the structure of the MoO_3 host. These compounds also possess metallic properties.

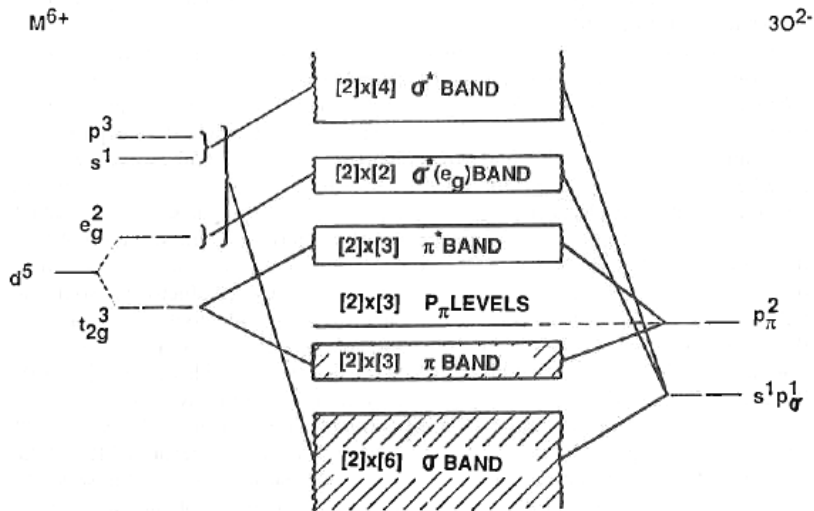


Fig. 2.1. Schematic Band Structure applicable to the bronzes [30].

2.1.2. Molybdenum trioxide (MoO₃)

Molybdenum trioxide (MoO₃), which is one of the two most stable oxides, can exist in two crystalline polymorphs form, the thermodynamically stable orthorhombic α -MoO₃ [35], and the metastable monoclinic β -MoO₃ phase [36-39].

α -MoO₃ is of orthorhombic symmetry (space group *Pbnm*) with $a = 3.963$ Å, $b = 13.855$ Å, and $c = 3.696$ Å and it has a layer structure. Each layer is comprised of infinite double ReO₃-chains which are linked together by equatorial edge-sharing to form zigzag slabs as shown in Figure 2.2(a). Each octahedron has one unshared corner and the corresponding oxygen atom is bonded to only one Mo cation. The MoO₆ octahedra exhibit a Jahn-Teller type distortion with four short and two long distances. MoO₃ does not contain any $4d$ electrons, and it therefore has insulating properties. Besides it is optically transparent due to its wide band gap.

While β -MoO₃ is similar to WO₃ and is related to the three-dimensional ReO₃ structure [36], which consists in corner-connected octahedra network, as shown Figure 2.2(b). It crystallizes with lattice constants $a = 7.122$ Å, $b = 5.366$ Å, $c = 5.566$ Å, and $\beta = 92.01$ (space group *P2₁/c*). The $\beta \rightarrow \alpha$ transformation is both exothermic and photochromic, with yellow β -MoO₃ convert to the white α phase above 400 °C at moderate heating rates [36]. The relatively high-transformation temperature implies that β -MoO₃ ought to have

a fair measure of kinetic stability at or near room temperature.

Meanwhile, band structure calculations for α - and β -MoO₃ were suggested by Sayede *et al.*, as shown in Figure 2.3a and b, respectively [40]. By the report, the calculated band gaps of α - and β -MoO₃ phase were 2.23 eV and 0.74 eV, respectively. Even though the energy gaps were smaller than experimental value (approximately 3.3 eV for α - MoO₃) and calculated one of the monoclinic structure with experimental parameters (1.01 eV for β -MoO₃)(there are no published values of the β -MoO₃ band gap), it is obvious that the band gap value of β -MoO₃ is quite small in comparison with that of the α -MoO₃. Therefore, β -MoO₃ is expected to be more conductive and less transparent than α -MoO₃.

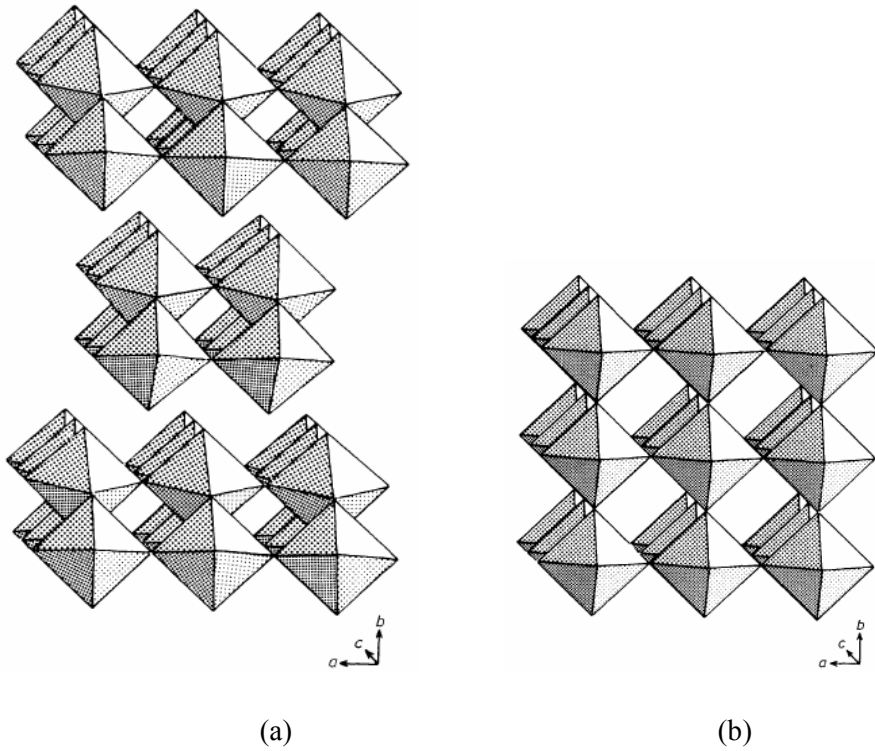
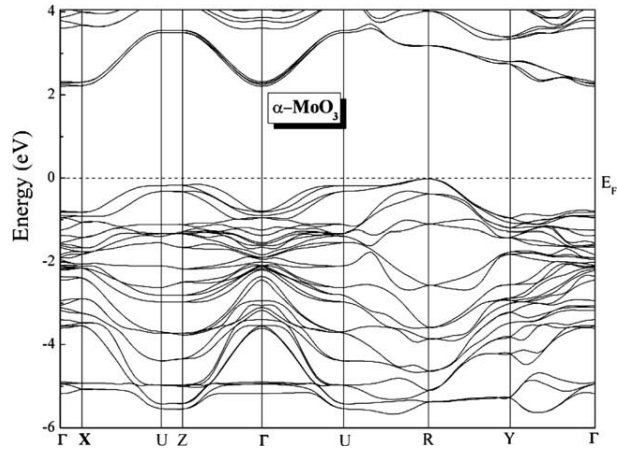
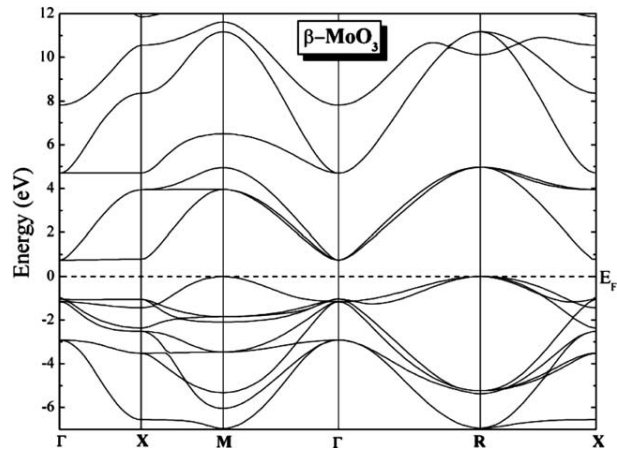


Fig. 2.2. An idealized representation of the structure of (a) α - MoO_3 and (b) β - MoO_3 [36].



(a)



(b)

Fig. 2.3. Valence and conduction band structure for (a) $\alpha\text{-MoO}_3$ and (b) $\beta\text{-MoO}_3$ in a typical orthorhombic reciprocal space path, all the high-symmetry positions of the first Brillouin zone. All energies $\epsilon(k)$ are taken with respect to the fermi energy [40].

2.1.3. Molybdenum dioxide (MoO₂)

This is the only molybdenum oxide structure which cannot be related to the ReO₃-chains. In order to describe the MoO₂ structure a different type of chains must be introduced, namely the rutile chains. These are infinite linear chains of edge-sharing octahedral, shown in Figure 2.4 [41]. The tetragonal structure of TiO₂ is comprised of such chains, which run along the four-fold axis and are linked together via corner-sharing along the other two directions. At room temperature MoO₂ has a monoclinic-distorted rutile structure (space group $P2_1/c$) with $a = 5.611 \text{ \AA}$, $b = 4.856 \text{ \AA}$, $c = 5.628 \text{ \AA}$, and $\beta = 120.9^\circ$. The Mo-Mo distance across the shared edge is very short, which indicates that the Mo cations are paired to form covalent bonds. This pairing causes a symmetry lowering from tetragonal to monoclinic, which allows the octahedral to have a sizeable distortion. The fact that MoO₂ has a metallic conductivity at all temperatures indicates that only one $4d$ electron of Mo⁴⁺ participates in the Mo-Mo covalent bonds (σ and π bonds). The other must participate in a Mo-O π conduction band responsible for the metallic conductivity [42,43].

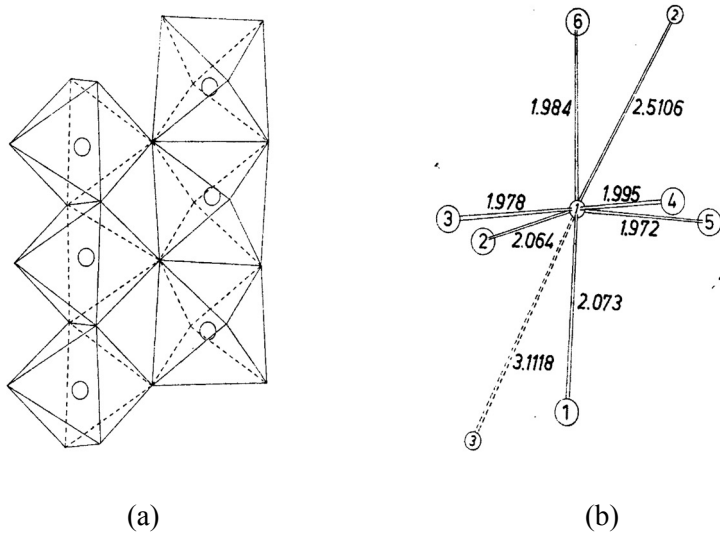


Fig. 2.4. (a) The structure of MoO_2 and (b) the coordination about the molybdenum atom showing the short Mo-Mo bonding [41].

2.1.4. Magnéli and related phases

Between MoO_2 and MoO_3 there exists a series of intermediate oxides, which have been synthesized and characterized from the crystallochemical point of view by Hägg, Magnéli and his collaborators as early as 1944 [44-48]. Later Kihlberg carried out a systematic structural study of the intermediate oxide series which includes seven members: $\text{Mo}_{18}\text{O}_{52}$, $\text{Mo}_{17}\text{O}_{47}$, Mo_9O_{26} , Mo_8O_{23} , Mo_5O_{14} , and two Mo_4O_{11} , the γ and η phases [49-56]. Except for the first two, the others belong to the series with the general formula $\text{Mo}_n\text{O}_{3n-1}$. As are the molybdenum bronze, some of these oxides are metallic conductors of low dimensionality.

The list of molybdenum oxides, which have been characterized from the crystallographic point of view, together with their crystallographic constants, are reported in Table 2-1[25]. Figure 2.5 shows the stability domain for each intermediate oxide according to Kihlberg [54]. In a review article [54] Kihlberg described the structure of all molybdenum oxides and classified them into three groups. The first includes the oxides of ReO_3 -type (with metallic behavior), namely Mo_8O_{23} , Mo_9O_{26} , $\gamma\text{-Mo}_4\text{O}_{11}$, and $\eta\text{-Mo}_4\text{O}_{11}$. The second group includes the oxides whose structure is of MoO_3 type, that is MoO_3 itself and $\text{Mo}_{18}\text{O}_{52}$. The third group includes the oxides which exhibit mixed polygonal networks, namely Mo_5O_{14} and $\text{Mo}_{17}\text{O}_{47}$.

Table 2-1. Crystal data of molybdenum oxides [25].

	a (Å)	b (Å)	c (Å)	β	<i>Space group</i>
Mo ₁₈ O ₅₂	8.145	11.89	21.23	67°8	$P\bar{1}$
	$\alpha = 102^\circ 67$		$\gamma = 109^\circ 97$		
Mo ₉ O ₂₆	16.75	4.030	14.45	96°0	$P2_1/a$
Mo ₈ O ₂₃	16.88	4.052	13.39	106°1	$P2_1/a$
Mo ₅ O ₁₄	46.00	23.00	3.937		$Pb2_1/a$
Mo ₁₇ O ₄₇	21.615	19.632	3.951		$Pba2$
η -Mo ₄ O ₁₁	24.54	5.439	6.701	94°3	$P2_1/a$
γ - Mo ₄ O ₁₁	24.49	5.457	6.752		$Pn2_1a$

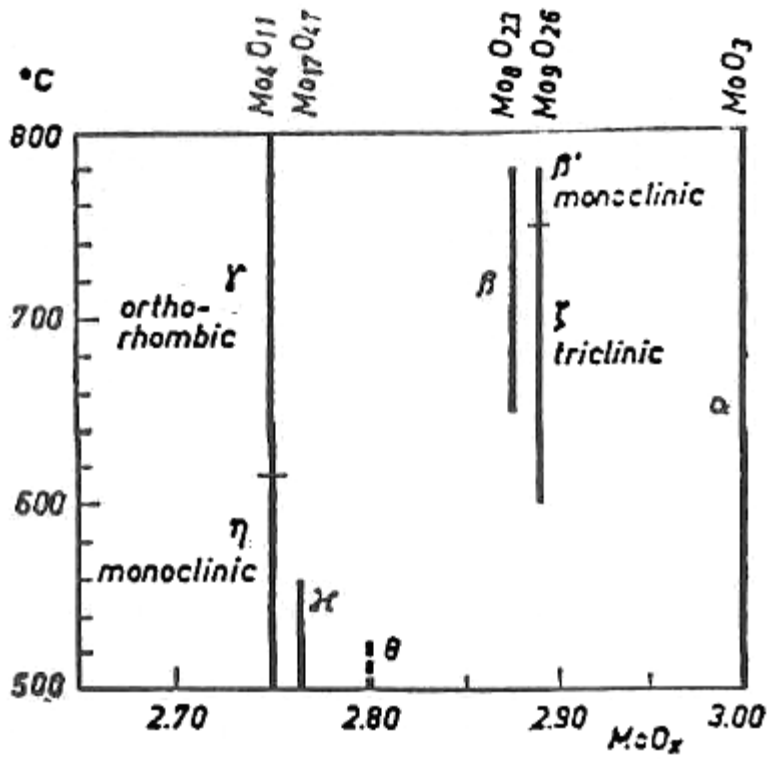


Fig. 2.5. Molybdenum oxides and their formation temperatures [54].

2.1.5. Hydrogen molybdenum bronzes (H_xMoO_3) [57]

Four different hydrogen molybdenum bronze phases were identified depending on the H atom concentration. Phases I ($0.25 < x < 0.40$) and II ($0.85 < x < 1.04$) are both blue in color with orthorhombic and monoclinic crystal structures, respectively. Phases III ($1.55 < x < 1.72$) and IV ($x = 2.0$) are monoclinic with red and green colors, respectively [58].

The calculated band structures and densities of states for several selected hydrogen bronzes are shown in Figure 2.6. In contrast to the semiconductor-like band structure of bulk α - MoO_3 , the band structures of all of the hydrogen bronzes exhibit strong metallic features with considerably widened valence bands across the Fermi level into the conduction bands. The abrupt change of electronic structures of the hydrogen bronzes arises from the strong H-bonding network formed upon H absorption and the subsequent charge transfer. The highly polarized bonding environment in the lattice gives rise to higher electron mobility, which makes the bronzes strongly metallic. This agrees well with the experimental findings, which shows that semiconducting molybdenum oxide becomes a metallic conducting hydrogen bronze upon H atom absorption [59].

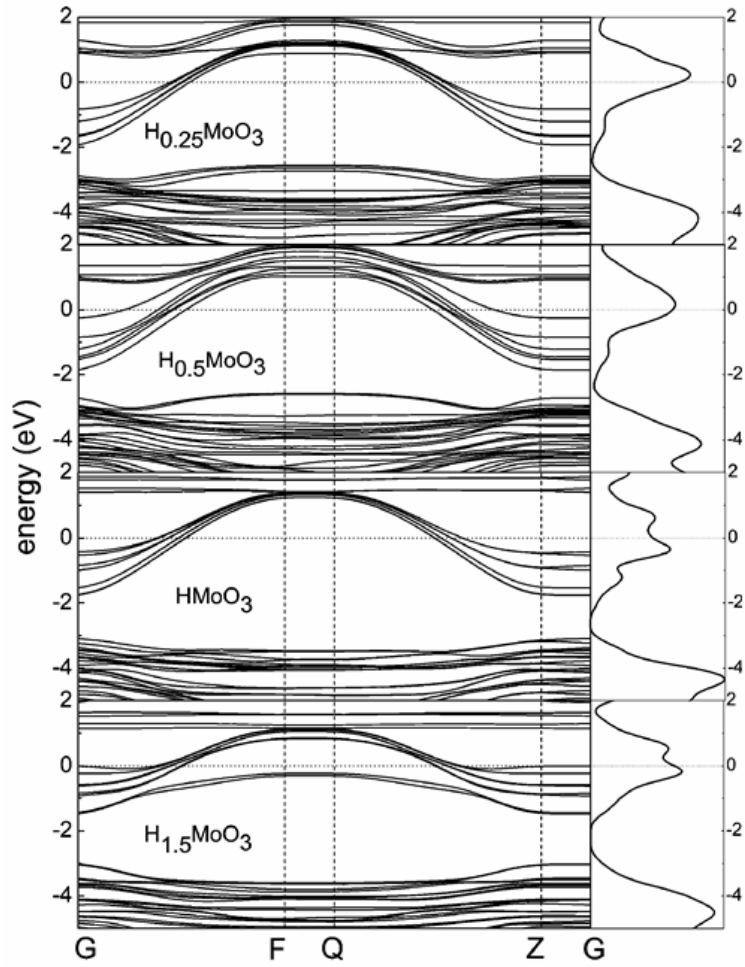


Fig. 2.6. Band structures and electronic densities of state for several hydrogen molybdenum bronzes, $\text{H}_{0.25}\text{MoO}_3$, $\text{H}_{0.5}\text{MoO}_3$, HMoO_3 , and $\text{H}_{1.5}\text{MoO}_3$. The energies are relative to the Fermi level [57].

2.2. Review on molybdenum-contained ternary oxides

The optoelectronic industries demand transparent conducting oxide (TCO) thin films, with high carrier mobility (μ). This is to increase the electrical conductivity (σ) without sacrificing optical transmission (T) for various applications [60,61]. Since indium tin oxide (ITO) films have low μ [62], many researches of novel TCOs with high μ have been performed as an alternative. Indium based oxide thin films were extensively studied in this aspect. High μ ($> 80 \text{ cm}^2 \text{ V}^{-1}\cdot\text{s}^{-1}$) Indium oxide films doped with metals such as titanium [63], zirconium [64], molybdenum (Mo) [65] and tungsten [66] were reported.

In particular, recently, it was reported that molybdenum-doped indium oxide (IMO) thin films, as prepared by thermal reactive evaporation, exhibited exceptional electrical and optical properties [65,67]. A low resistivity of $1.7 \times 10^{-4} \text{ } \Omega\cdot\text{cm}$, high mobility over $100 \text{ cm}^2\text{V}^{-1}\cdot\text{s}^{-1}$ and greater than 80% transparency were obtained [65,67]. While, electronic band structure investigations of IMO by Medvedeva revealed that the magnetic interactions which had never been considered to play a role in combining optical transparency with electrical conductivity ensure both high carrier mobility and low optical absorption in the visible range [68].

Meanwhile, Chen *et al.* reported first indium doped molybdenum oxide (In:MoO₃) as a new p-type TCO [69]. They produced In:MoO₃ single crystal

nanowires and amorphous films by sublimation of In_2O_3 and MoO_3 powders in tube furnace. Both nanowires and amorphous films exhibited high optical transmittance, 80–88% for 80 nm thick films at 400–800 nm wavelength, and low resistivity (down to $5.98 \times 10^{-4} \Omega \text{ cm}$). The electrical and optical values achieved are summarized in Table 2-2. After the report of Chen group, indium doped molybdenum oxide related researches have not been reported yet.

Table 2-2. Electrical and optical data of In:MoO₃ nanowire and thin films [69].

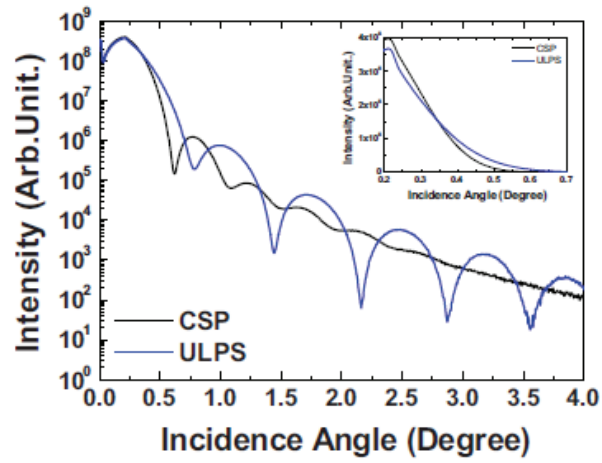
	<i>Resistivity</i> ($\Omega \cdot \text{cm}$)	<i>Mobility</i> ($\text{cm}^2 \text{V}^{-1} \cdot \text{S}^{-1}$)	<i>Carrier</i> <i>Concentration</i> (cm^{-3})	<i>Transmission</i> (400~800nm)
Nanowire	5.98×10^{-4}	-	-	61~74 %
Thin film (amorphous)	2.5×10^{-3}	11.9	3.0×10^{20}	80 ~88 %

2.3 Ultralow-pressure Sputtering Method

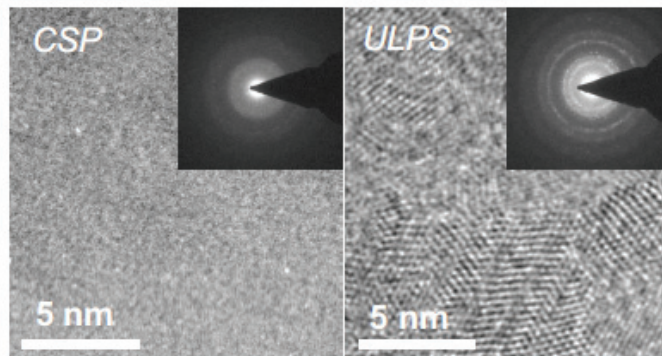
MoO_x films have been deposited by a variety of techniques, including thermal evaporation [70–72], electron beam evaporation [73], RF sputtering [74], dc reactive sputtering [75,76], sol-gel [77], spin coating [78], electrochemical deposition [79], aerosol assisted chemical vapor deposition [80] and hot filament metal oxide deposition [81]. Among the various deposition methods, pulsed laser deposition (PLD) seems to be the most proper method for transparent conducting oxide films since high-quality single crystals of thin films can be formed. Bhosle et al. also showed the high conductivity and high transmittance in the visible region for the PLD MoO_x films [26]. However, high temperature ambient during or after PLD deposition and non-uniform film thickness over a large substrate are disadvantageous to its extensive uses. In contrast, sputtering method can provide easy process control and uniform thickness and properties of films, thus it is the most widely used method in industry. But because as-deposited MoO_x films are amorphous phase, it is essential for the films to be crystallized in order to possess both transparent and conducting properties

Among the various parameters in the sputtering process, the sputtering pressure (SP) has the most influence on the crystal structure and surface morphology of the films. Especially, sputtering at low pressures of less than 1.3×10^{-1} Pa, the so-called ultra-low pressure sputtering (ULPS) method is

known to achieve films with a higher density and better crystallinity because the sputtered particles are more energetic than those at conventional sputtering pressures higher than 6.7×10^{-1} Pa [82,83]. ULPS method was first suggested by Huh *et al.* in order to obtain ITO films with smooth surface morphologies [83]. After that, Huh group also reported structural and electrical properties of SnO_x films produced by using ULPS method, in which the Hall mobility of the film was improved and the film was transformed from an amorphous structure to a nanocrystalline one [84]. Figure 2.7a and b shows the measured XRR data and HRTEM images for the tin-oxide (SnO_x) films deposited by CSP and ULPS [82]. The critical angle for the total external reflection for the ULPS-deposited SnO_x film was larger than for the CSP-deposited SnO_x film, indicating that the ULPS-deposited SnO_x film was denser than CSP, as shown in Figure 2.7a. The CSP-deposited SnO_x film had a density of 5.39 g/cm³, compared to an increased density of 5.77 g/cm³ for the ULPS-deposited SnO_x film. Figure 2.7b shows the HRTEM images of the SnO_x films deposited by CSP and ULPS. The diffraction patterns of the CSP-deposited SnO_x film represent the diffused rings indicating the amorphous phase, while the multiring pattern of the ULPS-deposited SnO_x film confirmed the nanocrystalline phase. Thus, the more energetic adatom energy arriving on the growing surface of the SnO_x film under the deposition condition of the ultralow sputtering pressure facilitated the densification of the SnO_x film, and, thereby, the formation of the nanocrystalline microstructure.



(a)



(b)

Fig. 2.7. Measured XRR data and HRTEM images for the SnO_x films deposited by CSP and ULPS. Each inset shows an enlarged graph of the XRR spectra and the diffraction patterns for the SnO_x films: (a) The measured XRR data and (b) the HRTEM images [82].

2.4. Figure of merit [85]

Both optical transmission and electrical conductivity of films should exceed a certain minimum value and should be as large as possible. However, the contemporaneous fulfillment of maximum transmission and conductivity is not possible due to their opposite relationship. Thus, in order to compare the performance of different transparent conducting materials, a figure of merit (F_{TC}) was defined by Fraser and Cook [86] and is given by

$$F_{TC} = \frac{T}{R_s} \text{ ----- (Eq. 2.1)}$$

where T is the optical transmission and R_s the electrical sheet resistance, which are given by the expressions below

$$T = I / I_0 = \exp(-\alpha t) \text{ ----- (Eq. 2.2)}$$

$$R_s = \frac{1}{\sigma t} \text{ ----- (Eq. 2.3)}$$

where I_0 is the radiation entering the film on one side and I is the radiation leaving the film on the other side, α is the optical absorption coefficient, t is the film thickness, and σ is the electrical conductivity.

Substituting the values of T (Eq. 2.2) and R_s (Eq. 2.3), respectively, in Eq. 2.1, we obtain

$$F_{TC} = \sigma / \exp(-\alpha t) \text{ ----- (Eq. 2.4)}$$

It is evident from this equation that the figure of merit of a film is a function of its thickness. The maximum value of F_{TC} corresponds to t_{max} which is calculated from

$$\frac{\partial F_{TC}}{\partial t} = \frac{\sigma \exp(\alpha t) - \sigma \alpha \exp(\alpha t)}{\exp(2\alpha t)} = 0$$

$$t_{max} = \frac{1}{\alpha} \text{ ----- (Eq. 2.5)}$$

Putting this value in Eq. 2.2, the optical transmission at maximum F_{TC} is given by

$$T = 1/e = 0.37 \text{ ----- (Eq. 2.6)}$$

This shows that the optical transmission reduces to 37 % for transparent conducting films with thicknesses corresponding to the maximum figure of merit. This value of transmission is too low for most transparent conductor applications.

In evaluating transparent conducting films based on F_{TC} , one particular film could be considered superior to others although its optical transmission is too low: this F_{TC} is thus too much in favor of sheet resistance. A better balance between optical transmission and sheet resistance has been achieved by

Haacke [65] who redefined the F_{TC} as

$$\begin{aligned}\phi_{TC} &= \frac{T^{10}}{R_s} \\ &= \sigma \exp(-10\alpha t) \text{----- (Eq. 2.7)}\end{aligned}$$

The maximum value of thickness that corresponds to the maximum value of the revised figure of merit ϕ_{TC} is given by

$$t_{\max} = \frac{1}{10\alpha} \text{----- (Eq. 2.8)}$$

The difference between ϕ_{TC} and F_{TC} is that maximum ϕ_{TC} occurs at 90 % optical transmission, whereas maximum F_{TC} occurs at only 37% optical transmission. This revised figure of merit ϕ_{TC} is widely used to compare the performance of various transparent conductors over a wide thickness range.

Table 2-3 compares the values of ϕ_{TC} for different films prepared by different techniques.

Table 2-3. Comparison of values of figure of merit ϕ_{TC} for different films

[85].

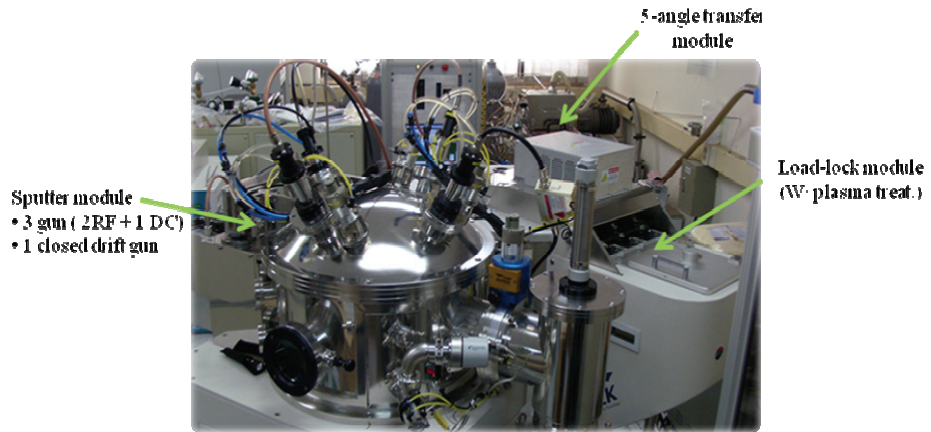
TCO	Deposition method	Sheet resistance ($\Omega \cdot \square^{-1}$)	Transmission (%)	ϕ_{TC} ($\Omega^{-1} \times 10^{-3}$)
SnO ₂	CVD	4.4	87	56.4
	Sputtering	600	75	0.1
SnO ₂ :F	Spray	18	88	15.4
In ₂ O ₃	Evaporation	6.75	90	51.6
	CVD	8.37	90	41.7
ITO	Sputtering	5	90	69.7
	Evaporation	22	90	15.8
Cd ₂ SnO ₄	Sputtering	14	93	34.6
ZnO	Sputtering	85	90	4.1
ZnO:Al	Sputtering	3.5-7.7	90	45.3-99.6
ZnO:Ga	Sputtering	33.3	85	5.9

III. Experiments and Analysis

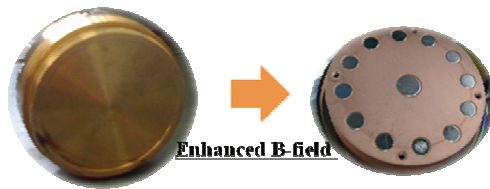
3.1. Sputter and furnace system for film preparation

Molybdenum oxide (MoO_x) and indium-doped MoO_x ($\text{In}:\text{MoO}_x$) films were deposited by dc magnetron reactive sputtering using a 5-angle cluster-type system (CS5000, SNTek Corp.). Figure 3.1(a) and (b) show the sputtering equipment with 5-angle cluster system and the modified cathode to enhance the magnetic field at the target surface compared to the general type. In detail, copper plate covering magnets planted in the cathode was removed and the distance between the center (N-pole) and edge (S-pole) magnets was minimized. Consequently, approximately 2-fold higher magnetic field could be obtained in the modified one and thus allows for even ultralow-pressure sputtering below 1.3×10^{-1} Pa [88].

Figure 3.2(a) and (b) show the furnace system (Thermo-tech Co. Ltd.) for post-deposition annealing (PDA) of MoO_x and $\text{In}:\text{MoO}_x$ films deposited by sputtering. By using a rotary pump, the base pressure can be obtained around 5×10^{-3} torr and usable gases are oxygen (O_2), nitrogen (N_2), and argon (Ar).



(a)

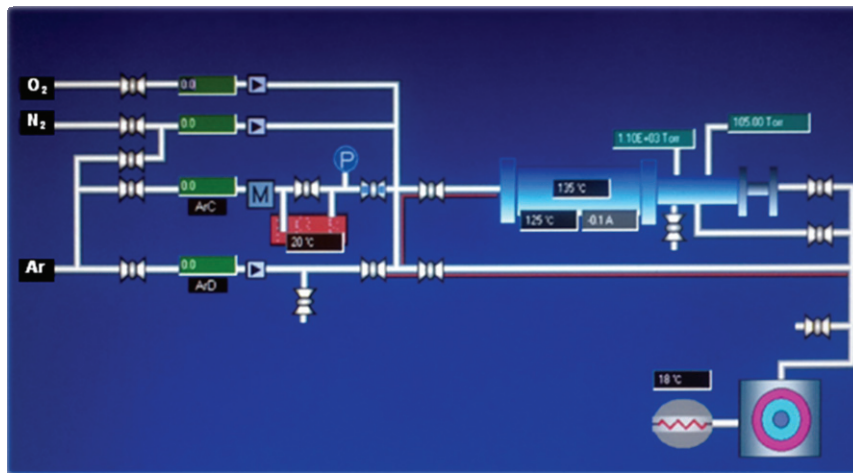


(b)

Fig. 3.1. The sputtering system with 5-angle cluster module; (a) a total image of sputtering equipments and (b) enhanced magnetic field structure of cathode (right) compared to the general type (left) [88].



(a)



(b)

Fig. 3.2. (a) Front-view of furnace system (b) schematic diagram of the apparatus for post-deposition annealing.

3.2. Resistivity and Hall effect [89]

The resistivity ρ is defined as the proportionality constant between the electric field E and the current density J :

$$E = \rho J \text{ ----- (Eq. 3.1)}$$

For semiconductors with both electrons and holes as carriers, we obtain

$$\rho = \frac{1}{q(\mu_n n + \mu_p p)} \text{ ----- (Eq. 3.2)}$$

If $n \gg p$, as in n-type semiconductors,

$$\rho = \frac{1}{q\mu_n n} \text{ ----- (Eq. 3.3a)}$$

$$\text{or } \sigma = q\mu_n n \text{ ----- (Eq. 3.3b)}$$

The most common method for measuring resistivity is the four-point probe method [90]. A small current from a constant-current source is passed through the outer two probes and the voltage is measured between the inner two probes. For a thin wafer with thickness W , the sheet resistance R_s is given by

$$R_s = \frac{V}{I} \cdot CF \quad (\Omega/\text{square}) \text{----- (Eq. 3.4)}$$

where CF is the correction factor. The resistivity is then

$$\rho = R_s W \quad (\Omega \cdot \text{cm}) \text{----- (Eq. 3.5)}$$

To measure the carrier concentration directly, the most common method uses the Hall effect [91]. Figure 3.3 shows the basic setup where an electric field is applied along the x axis and a magnetic field is applied along the z axis [92]. Consider a p-type sample. The Lorentz force $qv_x \times B_z$ exerts an average downward force on the holes, and the downward-directed current causes a piling up of holes at the bottom side of the sample, which in turn gives rise to an electric field E_y . Since there is no net current along the y direction in the steady state, the electric field along the y axis (Hall field) exactly balances the Lorentz force.

This Hall field can be measured externally and is given by

$$E_y = (V_y / W) = R_H J_x B_z \text{----- (Eq. 3.6)}$$

where R_H is the Hall coefficient and is given by [93]

$$R_H = r \frac{1}{q} \frac{p - b^2 n}{(p + bn)^2}, \quad b \equiv \mu_n / \mu_p \text{----- (Eq. 3.7)}$$

$$r \equiv \langle \tau^2 \rangle / \langle \tau \rangle^2 \text{----- (Eq. 3.8)}$$

The parameter τ is the mean free time between carrier collisions, which depends on the carrier energy, for example, for semiconductors with spherical constant-energy surfaces, $\tau \sim E^{-1/2}$ for phonon scattering, $\tau \sim E^{3/2}$ for ionized impurity scattering, and in general, $\tau = aE^{-s}$, where a (specimen width) and s (probe spacing) are constants. From Boltzmann's distribution for nondegenerate semiconductors, the average value of the m th power of τ is

$$\langle \tau^m \rangle = \int_0^\infty \tau^m E^{3/2} \exp(-E/kT) dE / \int_0^\infty E^{3/2} \exp(-E/kT) dE \text{----- (Eq. 3.9)}$$

so that using the general form of τ , we obtain

$$\langle \tau^2 \rangle = a^2 (kT)^{-2s} \Gamma\left(\frac{5}{2} - 2s\right) / \Gamma\left(\frac{5}{2}\right) \text{----- (Eq. 3.10)}$$

$$\langle \tau^2 \rangle = [a(kT)^{-s} \Gamma\left(\frac{5}{2} - 2s\right) / \Gamma\left(\frac{5}{2}\right)]^2 \text{----- (Eq. 3.11)}$$

where $\Gamma(n)$ is the gamma function defined as

$$\Gamma(n) \equiv \int_0^\infty x^{n-1} e^{-x} dx, \quad \Gamma\left(\frac{1}{2}\right) = \sqrt{\pi} \text{----- (Eq. 3.12)}$$

From the expression above we obtain $r = 3\pi/8 = 1.18$ for phonon scattering and $r = 315\pi/512 = 1.93$ for ionized impurity scattering.

The Hall mobility μ_H is defined as the product of the Hall coefficient and conductivity:

$$\mu_H = |R_H \sigma| \text{----- (Eq. 3.13)}$$

The Hall mobility should be distinguished from the drift mobility μ_n (or μ_p), as given in Eq. 3.3b, which does not contain the factor r . From Eq. 3.7, if $n \gg p$,

$$R_H = r \left(\frac{-1}{an} \right) \text{----- (Eq. 3.14)}$$

and if $p \gg n$,

$$R_H = r \left(\frac{+1}{qp} \right) \text{----- (Eq. 3.15)}$$

Thus the carrier concentration and carrier type (electron or hole) can be obtained directly from the Hall measurement provided that one type of carrier dominates.

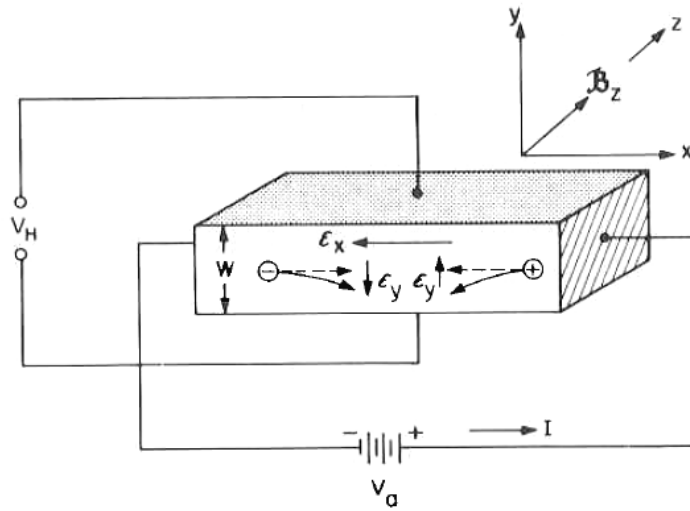


Fig. 3.3. Basic setup to measure carrier concentration using the Hall effect

[92].

3.3. Stress Measurement [94]

The experience techniques for measuring stresses in thin films on substrates fall into two general classes: (1) those based on direct measurements of the elastic strains in the films using X-rays and (2) those based on the associated curvature or deflection of the substrate. The direct X-ray techniques are most informative because they permit a measurement of all of the components of stress in the film. They can, in principle, be used to detect spatial variations of stress within the film, either from grain to grain or from one point in the film to another. They can also be used to find the stresses in patterned films with irregular geometries. However, because these techniques are based on diffraction, they are limited to crystalline films; they cannot be used to find the stresses in non-crystalline materials, such as passivation glasses or amorphous oxides. For these cases, the stresses must be determined by measuring the curvature or deflection of the substrate. Even for crystalline films, the substrate curvature technique is often preferable because it is more convenient to use and easier to apply to special conditions. Such conditions include *in situ* heating or cooling or stress measurements during the course of film growth.

The biaxial stress in a thin film on a much thicker substrate is directly proportional to the associated curvature of the substrate, provided the substrate deforms elastically. For the usual case of a substrate that is

elastically isotropic in the plane of the film, the expression for the biaxial stress in the film is

$$\sigma_f = M_s \frac{h_s^2}{6h_f} K = M_s \frac{h_s^2}{6h_f} \frac{1}{R} \text{----- (Eq. 3.16)}$$

and this is the Stoney formula, where $K = 1/R$ is the curvature of the substrate, M_s is the biaxial modulus of the substrate, and h_f and h_s are the thicknesses of the film and substrate, respectively [95]. The film stress does not depend on the properties or behavior of the film. This relation is valid for both elastic and plastic deformation in the film. In most cases, the bare substrate is not perfectly flat so that the curvature, K , in Eq. 3.16 [96] must be replaced by the change in curvature associated with the presence of the film. Thus, the stress in a film is found by measuring the curvature of the substrate both before and after the film is deposited or, equivalently, before and after the film is removed from the substrate.

A model for the generation of internal stress during the deposition of films is illustrated in Figure 3.4 [97].

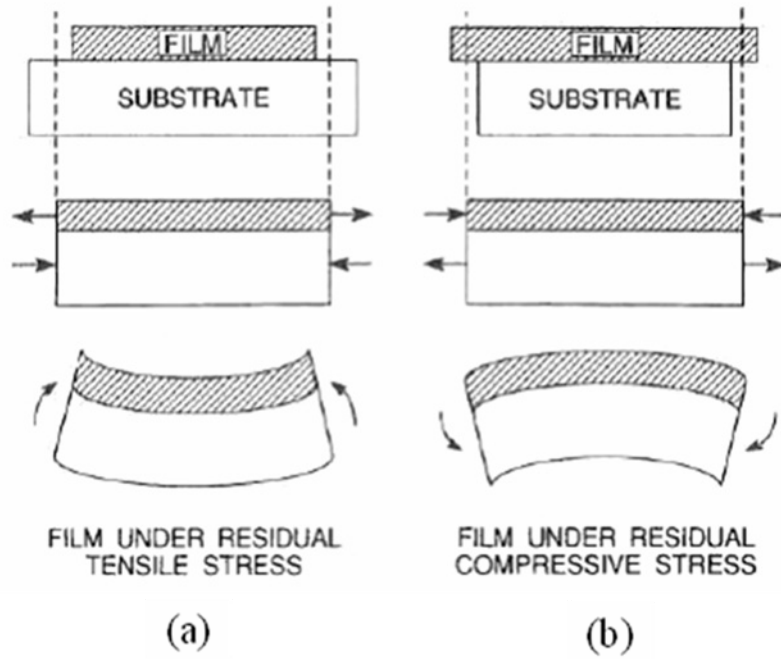


Fig. 3.4. Sequence of events leading to (a) residual tensile stress in film; (b) residual compressive stress in film [97].

3.4. Extraction of optical band-gap energy [98]

The optical absorption coefficient (α) was evaluated from the relation

$$\alpha = \frac{1}{t} \ln \left[\frac{T}{(1-R)^2} \right] \text{----- (Eq. 3.17)}$$

where T is the the transmittance, R the reflectance, and t the thickness of the film. The optical band gap (E_g) of the films was evaluated from the absorption coefficient by fitting the data to

$$\alpha h\nu = B(h\nu - E_g)^{1/2} \text{----- (Eq. 3.18)}$$

where $h\nu$ is the photon energy and B the edge width parameter.

The films formed at room temperature show high transmission without significant absorption around 800 nm. The evaluated band gap of the films formed at room temperature has been reported to around 3.2 ~3.3 eV [98]. The optical transmission above the absorption edge decreases with increasing substrate temperature with a slight shift in the absorption edge towards the higher wavelength region.

3.5. Analysis Methods

Several measurement techniques were employed to analyze the structural, electrical, chemical, and optical properties of the TCO films: The thickness of the films was measured simply by both single-beam ellipsometry (L116S300, Gaertner Scientific Corp.). To evaluate the surface morphology and surface roughness of the films, field emission scanning electron microscopy (FE-SEM, S-4800, Hitachi) and atomic force microscopy (AFM, XE-150, PSIA) were utilized. Nomarski (or DIC) microscopy was also employed to obtain three-dimensional surface images with apparent shadows (ECLIPSE LV100D, Nikon). Glancing angle X-ray diffractometry (XRD, X'Pert PRO, PANalytical) was carried out using Cu K α radiation at 40 kV and 30 mA to determine the structures of the films and high-resolution X-ray reflectivity (XRR) measurements were also performed using the same system with XRD to confirm the density of the films. The high-resolution images of films were also obtained by high-resolution transmission electron microscopy (HRTEM, Tecnai F20, FEI). The compositions and chemical properties of the films were analyzed by X-ray fluorescence (XRF, ARL Quant'X EDXRF, Thermo Scientific), Rutherford backscattering spectroscopy (RBS, 6SDH-2, NEC) and X-ray photoelectron spectroscopy (XPS, SIGMA PROBE, Thermo VG), respectively. XPS raw data were calibrated by C 1s peak to 284.5 eV. Additionally, the depth profiles of elements in the films were analyzed by

Auger electron spectroscopy (AES, Perkin-Elmer, Model-660). A stress measurement system (FLX 2320, KLA TENCOR) was used in order to measure the residual stress of MoO_x films deposited on the (100) Si 4 inch full wafers. The electrical resistivity, carrier concentration, and Hall mobility were measured by Hall-effect measurement system with van der Pauw geometry (HL5500PC, BIO-RAD), in which the magnetic field was fixed at 0.5 T. The optical transmittance of the films was measured by an UV-VIS single-beam spectrometer (CARY5000, VARIAN).

3.6. Deposition of MoO_x Films (chap. 4.1- 4.2)

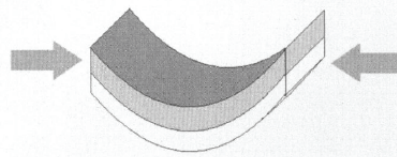
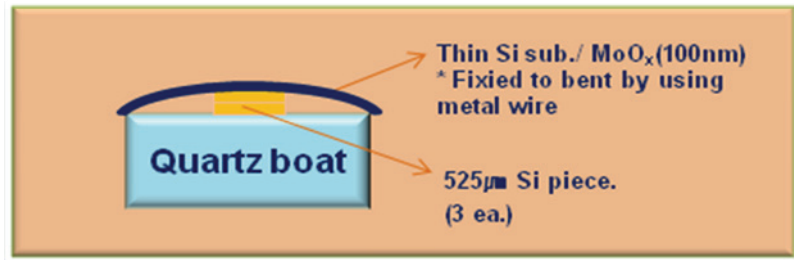
The MoO_x thin films were deposited on Si (100) wafers, SiO₂(100nm)/Si wafers and Corning 1737 glass substrates by the reactive DC magnetron sputtering method. The sputtering system was a five-angle cluster-type system (CSP5000, SNTek Corp.), as explained previously in section 3.1. A metallic Mo target (99.95 %, LTS Inc.) with 7.5 cm diameter was sputtered in an oxygen (O₂) and argon (Ar) gas mixture, whose O₂ content was varied from 10 to 40 %, controlled by regulating the oxygen flow. Sputtering pressures were adjusted by finely controlling throttle valve. The thickness of the MoO_x film was approximately 100 nm. The applied DC power was fixed at 100 W (2.2 W/cm²) and the distance between the target and substrate was 12 cm. The base pressure was 8.0×10^{-5} Pa. The post-deposition annealing (PDA) was carried out in argon (Ar) ambient in the temperature of from 250 °C to 450 °C for 2 or 8 hours.

In order to measure the film stress of MoO_x, Si (100) full 4-inch wafers were used. Generally, as the bare substrate is not perfectly flat, the curvature of the substrate both before and after the film is deposited were measured for all wafers.

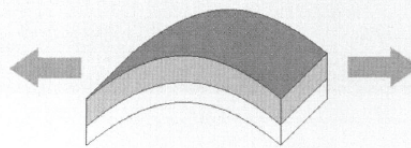
For the experiment of section 4.1.4, 100 μm-thick Si wafers with bendable property were used. 100nm-thick MoO_x films were deposited in the sputtering pressure of 1.3×10^{-1} Pa. To let the film be under consistent compressive or

tensile stress during post-deposition annealing, the MoO_x(100 nm)/Si(100 μm) stacked 3cm×3cm specimen was fixed to bent on quartz boat by using metal wire, as shown in Fig. 3.5.

The specifications of detailed deposition conditions for MoO_x films were summarized in Table 3-1.



(Compressive stressed film)



(Tensile stressed film)

Fig. 3.5. Schematic diagram for bending of MoO_x(100 nm)/Si(100 µm) stacks.

Table 3-1. Detailed deposition and PDA conditions for MoO_x films.

	ULPS film	CSP film
Target	Mo (<i>putity</i> :99.95 %)	
Initial Pressure (Pa)	< 8.0×10 ⁻⁵	
Sputtering Pressure (Pa)	6.7×10 ⁻² , 1.3×10 ⁻²	6.7×10 ⁻¹
Target-Substrate Distance (cm)	12	
Substrate Rotation Rate (rpm)	24~26	
Substrate Temperature	Room Temperature	
Gas Flow (sccm)	Ar + O ₂ = 10 (O ₂ : 1 ~ 4sccm (10 % ~ 40 %))	
Sputtering Power (W/cm ²)	2.2 (100W)	
PDA temperature (°C)	250 ~ 450 (interval 50 °C)	

3.7. Deposition of In:MoO_x Films (chap. 4.3)

The Indium-doped MoO_x (In:MoO_x) thin films were deposited on Si (100) wafers, SiO₂(100nm)/Si wafers and Corning 1737 glass substrates by the reactive DC magnetron sputtering method. MoIn compound target was simply made by attaching indium chip (99.99 %, Kojundo) on a metallic Mo target (99.95 %, LTS Inc.) with 7.5 cm diameter, as shown in Fig. 3.6. For good adhesion between In and Mo, the target was heated up to 190°C ~ 200°C on hot-plate, and then cooled slowly in air. The content of indium in In:MoO_x films was changed by varying the number or location of indium chips attached on Mo target. The produced MoIn target was sputtered in O₂ and Ar gas mixture, whose O₂ content was varied from 20 % to 40 %. The thickness of the MoO_x film was approximately 100 nm. The applied DC power was fixed at 100 W (2.2 W/cm²) and the distance between the target and substrate was 12 cm. The base pressure was around 8.0×10^{-5} Pa. The post-deposition annealing (PDA) was carried out in Ar ambient in vacuum furnace at the temperature from 250 °C to 450 °C for 2 hours.

The specifications of detailed deposition conditions for MoO_x films were summarized in Table 3-2.

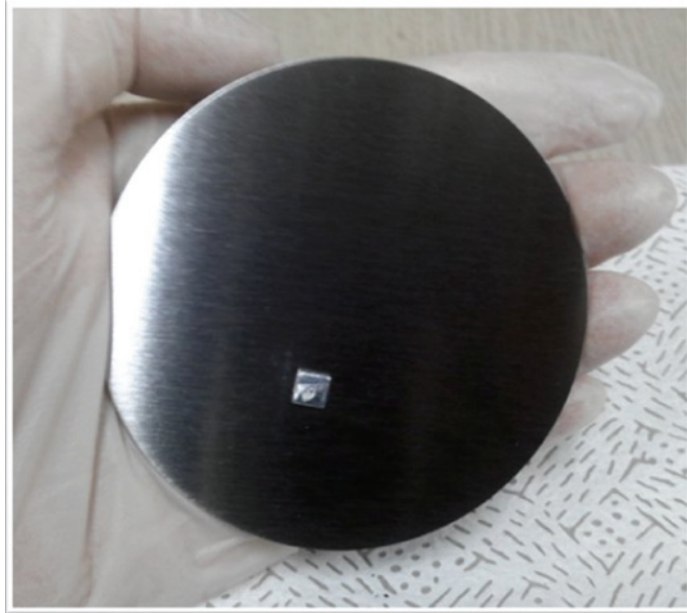


Fig. 3.6. Photograph for MoIn metallic target: One indium chip was attached on Mo target.

Table 3-2. Detailed deposition and PDA conditions for In:MoO_x films.

	In:MoO _x
Target	Indium chip attached Mo (Mo:99.95%, In:99.99%)
Initial Pressure (Pa)	$< 8.0 \times 10^{-5}$
Sputtering Pressure (Pa)	6.7×10^{-1}
Target-Substrate Distance (cm)	12
Substrate Rotation Rate (rpm)	24~26
Substrate Temperature	Room Temperature
Gas Flow (sccm)	Ar + O ₂ = 10 (O ₂ : 2 ~ 4sccm (20 % ~ 40 %))
Sputtering Power (W/cm ²)	2.2 (100W)
PDA temperature (°C)	250 ~ 450 (interval 50 °C)

IV. Results and Discussions

4.1. Effects of sputtering pressure on the TCO properties of MoO_x films

4.1.1. Deposition characteristics

Figure 4.1 shows the dependence of the deposition rate on the O₂ (%) contents in the sputtering gas (Ar + O₂) at sputtering pressures of 6.7×10^{-1} , 1.3×10^{-1} , and 6.7×10^{-2} Pa. The deposition rate decreased with increasing O₂ content in the sputtering gas, regardless of the sputtering pressure. This behavior is well known to be caused by three factors: a target poisoning by oxygen atoms [99], the less efficient sputtering of the target by oxygen ions compared to Ar ions [100], and negative ion impingement on the growing film surface [101]. In this system, the target poisoning and higher sputtering yield of Ar ions seem to determine the deposition rate. At a low O₂ content, the high sputtering yield due to the high Ar content dominated over the low level of target poisoning, resulting in the highest deposition rate being obtained at the highest sputtering pressure, 6.7×10^{-1} Pa. Meanwhile, at a high O₂ content, the target poisoning overwhelmed the sputtering yield of Ar, with the result that the highest deposition rate occurred at the lowest pressure of 6.7×10^{-2} Pa. Interestingly, the deposition rate at higher pressure was affected more by the

O₂ content: the deposition rate at the highest pressure, 6.7×10^{-1} Pa, steeply decreased with increasing O₂ content. This can be attributed to the severer target poisoning due to more O₂ molecules existed in higher pressure even at the same O₂ content. A similar result was reported by Suzuki et al., who described the relationships between the deposition rate and some sputtering parameters for Sb-doped SnO₂ films [102].

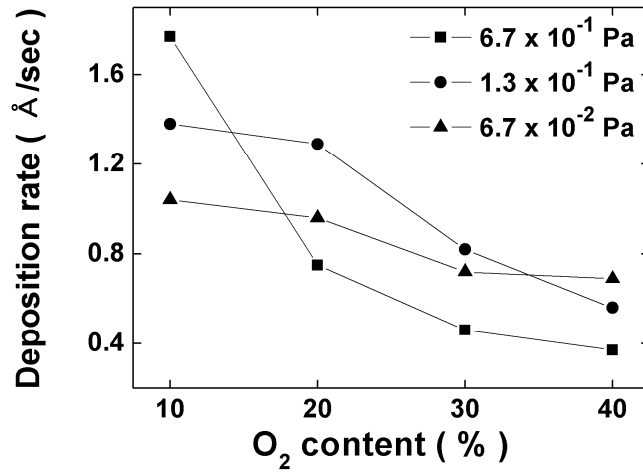


Fig. 4.1. Deposition rate of MoO_x films as a function of the O₂ content (%) in the sputtering gas (Ar + O₂) at the sputtering pressures of 6.7×10^{-1} , 1.3×10^{-1} , and 6.7×10^{-2} Pa.

4.1.2. Structural properties

Figure 4.2 shows the X-ray diffraction patterns of the as-deposited and PDA (at 450 °C for 8 h in Ar ambient) MoO_x films. The as-deposited films deposited at sputtering pressures of 6.7×10^{-1} Pa (Fig. 4.2(a)) and 1.3×10^{-1} Pa (Fig. 4.2(b)) were almost amorphous, regardless of the O₂ content, even though those deposited at a pressure of 1.3×10^{-1} Pa (Fig. 4.2(b)) had a weak monoclinic (102) MoO₂ peak. However, the ULPS MoO_x films deposited at 6.7×10^{-2} Pa showed a quite different pattern (Fig. 4.2(c)): regardless of the O₂ content, the films contained a weak but sharp monoclinic (-203) MoO₂ peak and, in the case where the O₂ content was 10 %, the film contained Mo bcc phase as well as the MoO₂ monoclinic phase. These results indicate that the ULPS MoO_x films are better crystallized than those sputtered at normal-pressure, due to the more highly energetic ions at the lower pressure, and that the crystal structure of the films is strongly dependent on the sputtering pressure [77]. For the PDA MoO_x films, several diffraction peaks appeared, as shown in Figs. 4.2(d) - (f), indicating that they were well crystallized through the annealing process, but that different crystal phases evolved in each PDA MoO_x film depending on the sputtering pressure and O₂ content. The monoclinic MoO₂ phase was observed at O₂ contents of 10 %, 20 % and 30 % and sputtering pressures of 6.7×10^{-1} Pa, 1.3×10^{-1} Pa and 6.7×10^{-2} Pa, respectively, and the position of the monoclinic MoO₂ peaks was almost the

same. However, the peak intensity increased with decreasing sputtering pressure and, consequently, the strongest peak intensity was observed in the case of the ULPS MoO_x film. This indicates that the crystallinity of the PDA MoO_x film deposited by lower pressure sputtering was much improved. This result is very similar to that reported by Wang et al [103,104]. They deposited molybdenum nitride films by reactive sputtering and discussed the evolution of the crystal structure with the sputtering pressure from the kinetic point of view, insisting that the higher deposition rate at a higher sputtering pressure restricted the atomic arrangement and thus developed an amorphous phase. Even though their proposed mechanism can explain the crystallization result quite well, it does not provide a complete explanation for the high crystallization behavior of the PDA ULPS MoO_x films in this work. Besides the kinetic mechanism, another reasonable one is needed to explain it. Huh *et al.* [88] reported that the energy of the sputtered particles arriving at the substrate (E_F) was calculated about 65 % higher for ULPS than for normal-pressure sputtering. More energetic particles sputtered in the ULPS condition are bombarding the growing film, resulting in an increase of MoO_x film density. The highly dense film mostly induces high compressive residual strain, which can enhance their crystallization [105]. Meanwhile, the ULPS MoO_x film, deposited at a high O₂ content, included MoO₂, MoO₃ (β -MoO₃) and Magnéli (monoclinic structure only) phases. On the other hand, those deposited at high pressures of 6.7×10^{-1} and 1.3×10^{-1} Pa, contained mainly

insulating orthorhombic MoO_3 phase together with a small amount of monoclinic phase.

Figure 4.3 shows the composition variations of the MoO_x films, which were determined by RBS, as a function of the sputtering pressure at various O_2 contents. The O/Mo atomic ratio of the MoO_x films decreased with decreasing sputtering pressure at the same O_2 content. This can be explained by considering the deposition mechanism of reactive sputtering. As mentioned above, more target poisoning occurs due to the increased number of O_2 molecules with increasing sputtering pressure at the same O_2 content. Thus, MoO_x molecules with high O/Mo atomic ratio may be sputtered out and transported to the substrate, resulting in oxygen-rich MoO_x films at higher sputtering pressures. As a consequence, the composition of the sputtered MoO_x films can be controlled by adjusting the sputtering pressure and O_2 content: stoichiometric MoO_2 films (the lower dotted line at an O/Mo ratio ≈ 2.0) can be achieved at 6.7×10^{-1} Pa, 1.3×10^{-1} Pa, and 6.7×10^{-2} Pa at 10 %, 20 % and 30 % O_2 contents, respectively. The stoichiometric composition of the MoO_2 films was also confirmed by the formation of monoclinic MoO_2 phase in the XRD pattern, as shown in Fig. 4.2. MoO_x films with an oxygen-rich composition (the upper dotted line at an O/Mo ratio ≈ 2.85) also developed at 6.7×10^{-1} Pa, 1.3×10^{-1} Pa, and 6.7×10^{-2} Pa at O_2 contents of 30 %, 30 % and 40 %, respectively.

Figures 4.4(a) and (b) show the measured XRR data for two groups of films

with ratios of $O/Mo \approx 2.0$ and $O/Mo \approx 2.85$, respectively. A shift in the total reflection edge, which implied a change in the density, was observed in both Figs. 4.4(a) and (b) [106]. Fig. 4.4(c) exhibits the density of each film acquired by XRR data-fitting. The upper curve is for the as-deposited MoO_x films with $O/Mo \approx 2.0$ and the lower one is for those with $O/M \approx 2.85$. In both of them, the density of the films increased with decreasing sputtering pressure and reached the highest value for the ULPS MoO_x films. Generally, energetic particle bombardment causes “atomic peening”, which leads to the densification of the material and also introduces a compressive stress in the film [107]. The ULPS MoO_x films were under higher compressive stress than the films sputtered at a the normal pressure of 6.7×10^{-1} Pa and a higher compressive stress was built up for the stoichiometric films ($O/Mo \approx 2.0$) than for the oxygen-excess films, as shown in Fig. 4.5. During annealing, these high stresses in the as-deposited ULPS MoO_x films may act as the driving force to promote their crystallization [108]. Therefore, the stress and density of the as-deposited MoO_x films seem to be the key factors determining the crystallization of the films before or after PDA.

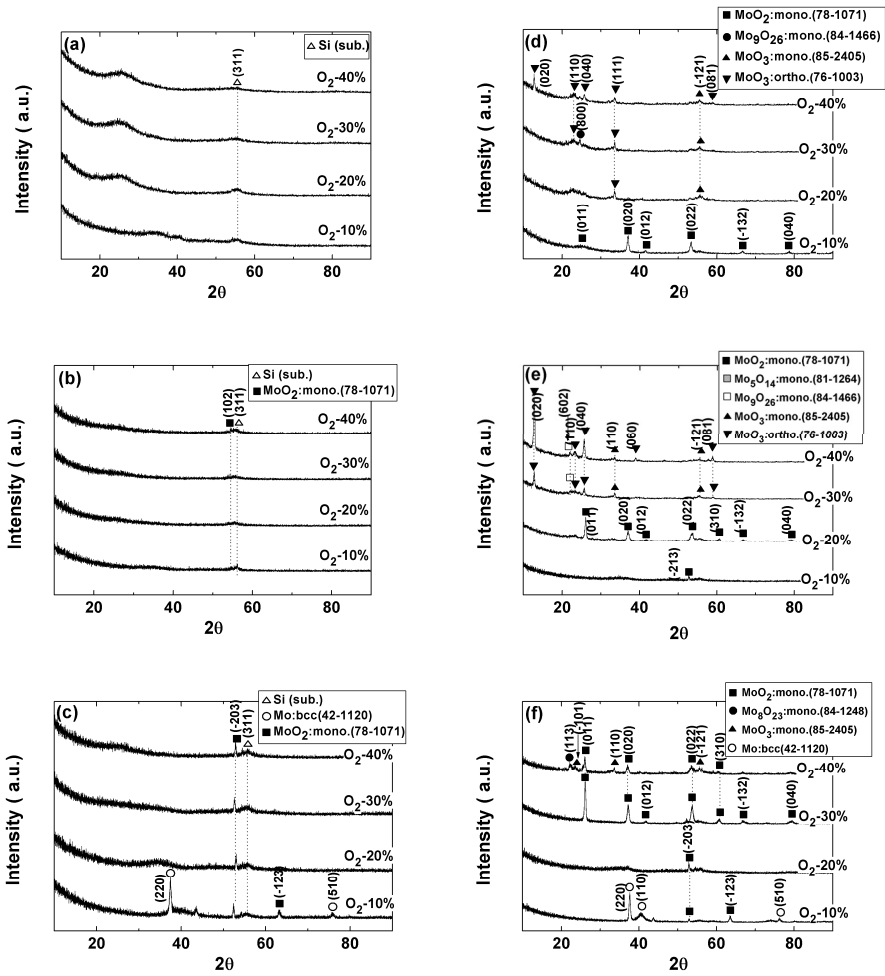


Fig. 4.2. XRD patterns of as-deposited and PDA MoO_x films (at 450°C for 8 h in Ar ambient) in the sputtering pressure of (a) and (d) 6.7×10^{-1} Pa, (b) and (e) 1.3×10^{-1} Pa, and (c) and (f) 6.7×10^{-2} Pa, respectively, at the O_2 contents of 10, 20, 30, and 40 %.

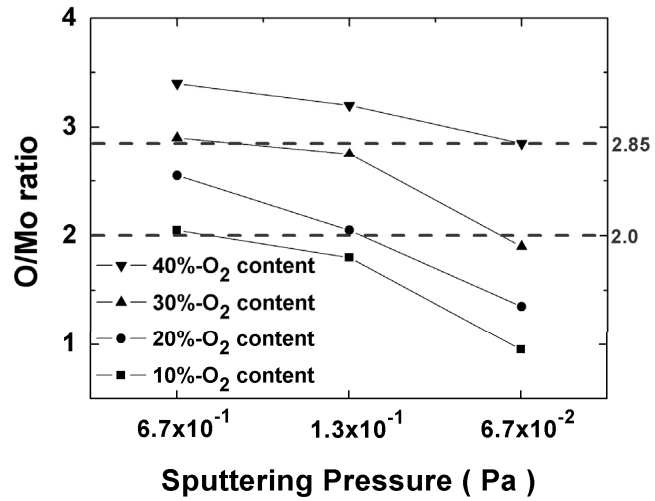


Fig. 4.3. O/Mo ratio of the PDA MoO_x films, which was analyzed by RBS, as a function of the sputtering pressure at O₂ contents of 10 %, 20 %, 30 %, and 40 %.

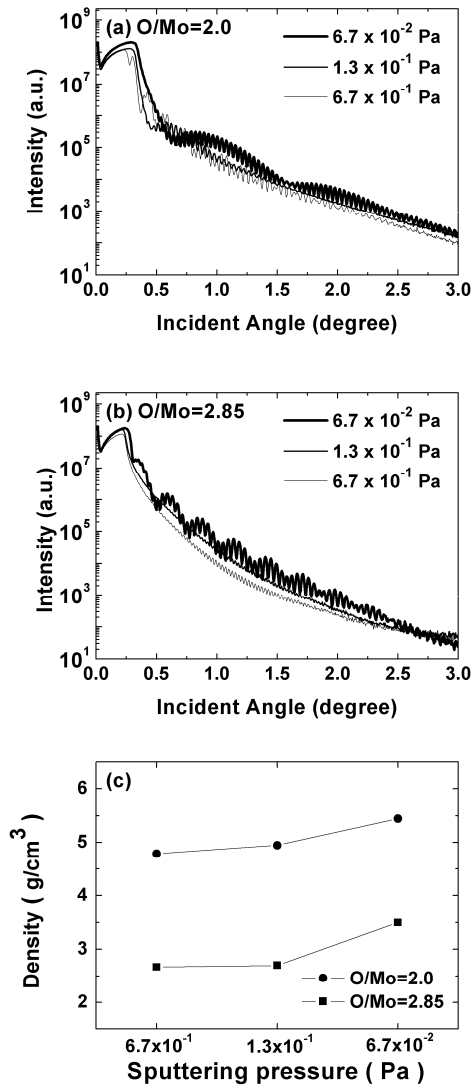


Fig. 4.4. Measured XRR data for (a) $O/Mo \approx 2.0$ and (b) $O/Mo \approx 2.85$, and (c) the variation of density of as-deposited MoO_x films with $O/Mo \approx 2.0$ and 2.85 as a function of sputtering pressure.

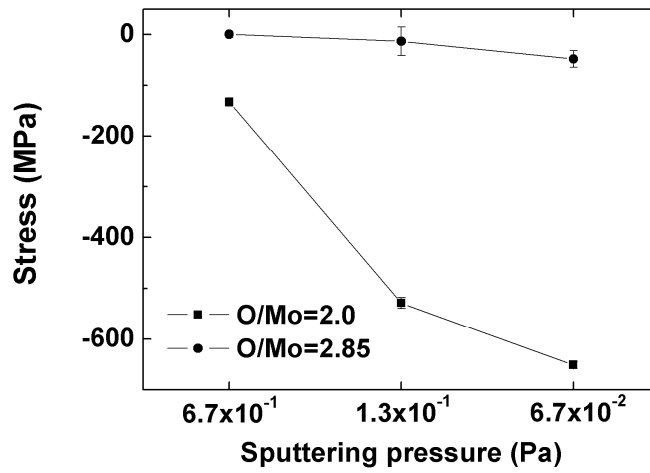


Fig. 4.5. Stress in as-deposited MoO_x films for $\text{O}/\text{Mo} \approx 2.0$ and 2.85 as a function of sputtering pressure.

4.1.3. Electrical and Optical properties

Figure 4.6 shows the dependence of the electrical resistivity (ρ) of the as-deposited and PDA MoO_x thin films. Each point, measured by Hall-effect measurement, is the average value of five measurements for each sample. The points, which are not shown in the upper part of graph, exceed the measurement limit. The PDA MoO_x films exhibit a lower resistivity, higher carrier concentration and higher carrier mobility than those of the as-deposited films, due to their improved crystallinity, as shown in Fig 4.2. As the O_2 content increased, the resistivity monotonically increased in the case of a pressure of 6.7×10^{-1} Pa, while it reached a minimum at O_2 contents of 20 % and 30 % for pressures of 1.3×10^{-1} Pa and 6.7×10^{-2} Pa, respectively, and then increased. Similar behavior of the resistivity with the O_2 content was reported in the case of various oxides such as SnO_2 , F-doped SnO_2 and Sn-doped In_2O_3 [109-118]. Srinivasa et al. investigated the effect of the O_2 flow rate, $F(\text{O}_2)$, on the sheet resistance (R_s) of SnO_2 films grown by a CVD technique. They reported that the relatively high value of R_s for low values of $F(\text{O}_2)$ was due to the presence of highly resistive SnO and/or Sn_3O_4 phases, and the decrease in the concentration of these phases with the initial increase in $F(\text{O}_2)$ resulted in a decrease of R_s . They also stated that the minimum R_s was reached when the SnO_2 films had the optimum concentration of oxygen vacancies [111]. As seen in Fig. 4.2, the well-crystallized MoO_x films having

the largest proportion of monoclinic MoO₂ phase, which were deposited under the conditions of 10 % O₂ at 6.7 x 10⁻¹ Pa, 20 % O₂ at 1.3 x 10⁻¹ Pa and 30 % O₂ at 6.7 x 10⁻² Pa, exhibited the minimum resistivity. In the case of the ULPS condition of 6.7 x 10⁻² Pa, the films having the highest MoO₂ peak intensity in their XRD patterns showed the lowest resistivity value. However, unlike the SnO₂ films with the minimum resistivity due to its having the optimum concentration of oxygen vacancies, the low resistivity of the MoO₂ phase is due to the nature of MoO₂ itself, that is MoO₂ has only one 4d electron of Mo⁴⁺ participating in the Mo-Mo covalent bonds (σ and π bonds), while the other participates in the Mo-O π conduction band responsible for the metallic conductivity of MoO₂ [42,119,120]. This result is confirmed by the Hall-effect measurement results plotted in Fig. 4.7.

Figure 4.7 shows the variations of the electrical resistivity (ρ), Hall mobility (μ), and carrier concentration (n) of the PDA MoO_x films deposited at a sputtering pressure of 6.7 x 10⁻² Pa with the O₂ content. The carrier concentration (n) initially decreased up to an O₂ content of 20 %, but then increased rapidly and ultimately reached a maximum value of $2.4 \times 10^{22} \text{ cm}^{-3}$ at an O₂ content of 30 %. However, the Hall mobility at an O₂ content of 30 % was very low. This may be due to ionized impurity scattering, which is the dominant scattering mechanism when the carrier concentration is greater than 10^{20} cm^{-3} [119].

Figure 4.8(a) exhibits the optical transmittance (%) for the same sample as

that in Fig. 4.7. A gradual increase of the transmittance was observed as the O₂ content increased up to 40 %, which was quite a different trend from the variation of the resistivity. The maximum value of the transmittance within the 400-500 nm wavelength range in the case of an O₂ content of 40 % was about 73 %. Fig. 4.8(b) shows that for the MoO_x films with the same O/Mo atomic ratio (≈ 2.85), as the sputtering pressure increased, the optical transmittance line shifted upwards. Considering both the resistivity and optical transmittance, it can be concluded that the PDA MoO_x film deposited under the sputtering conditions of 6.7×10^{-2} Pa and 40 % O₂, was most suitable for transparent conductive MoO_x. We summarize the present and previously reported results [26] in Table 4-1. From the comparison of the performance of the film with that of the previously reported one, it can be said that the result in this experiment is encouraging, since the sputtering process is more versatile for mass production. Even though this result still does not reach the level of electrical and optical performance of commercial indium tin oxide (ITO) (%T >80, $\sim 10^{-4} \Omega \cdot \text{cm}$), more process adjustment may provide the required enhancement of both the transmittance and conductivity.

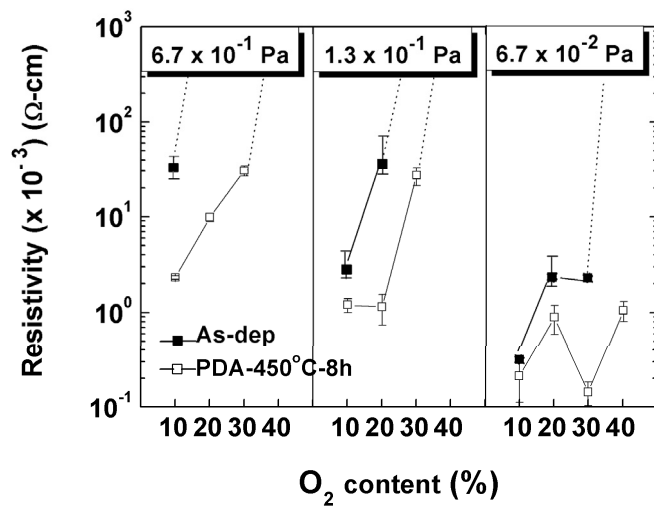


Fig. 4.6. Dependence of the electrical resistivity (ρ) on O_2 content in the sputtering pressures of 6.7×10^{-1} , 1.3×10^{-1} , and 6.7×10^{-2} Pa; closed squares denote ρ values of as-deposited MoO_x films and open squares denote those of PDA MoO_x films.

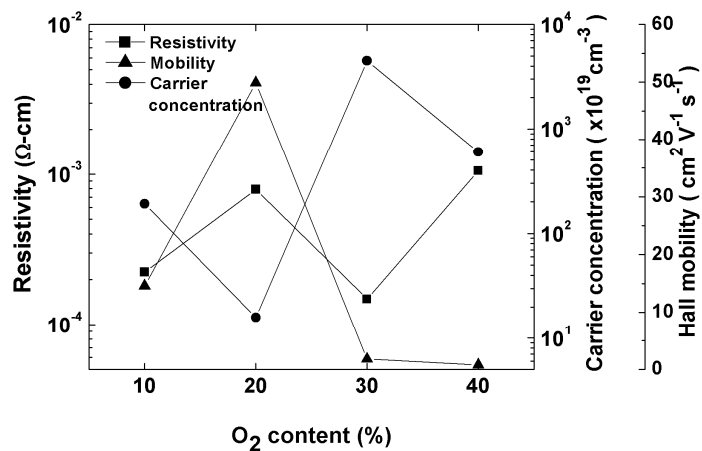


Fig. 4.7. Variation of the electrical resistivity (ρ), Hall mobility (μ), and carrier concentration (n) of PDA MoO_x films (450°C , 8 h, Ar) with the O_2 content in sputtering ambient. The sputtering pressure was 6.7×10^{-2} Pa.

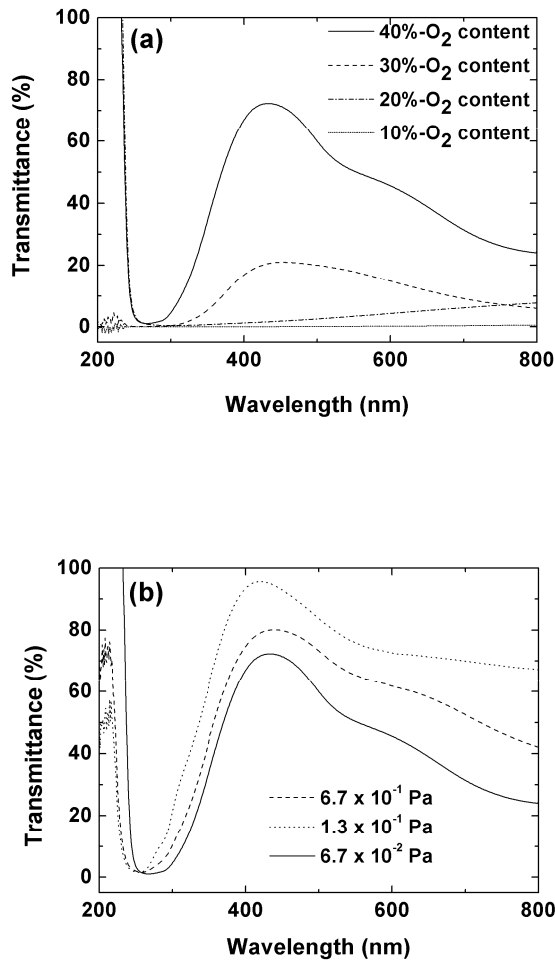


Fig. 4.8. Optical transmittance as a function of wavelength: (a) PDA-ULPS MoO_x films (sputtering pressure 6.7 x 10⁻² Pa) with various O₂ contents and (b) PDA MoO_x films deposited in various sputtering pressures (The ratio of O/Mo is about 2.85).

Table 4-1 Comparison of optical and electrical properties of MoO_x films deposited by reactive sputtering and pulsed laser deposition.

Sample	Deposition method	Deposition temp.	PDA conditions		Transmittance (%)	Resistivity (Ω·cm)	Film thickness (nm)
			Temp. (°C)	Holding time (h)			
Present result	Reactive sputtering	RT	450 °C	8	73	1.05 x 10 ⁻³	100
Ref. [26]	Pulsed laser deposition	550 °C	250 °C	1	65.1	1.00 x 10 ⁻³	60

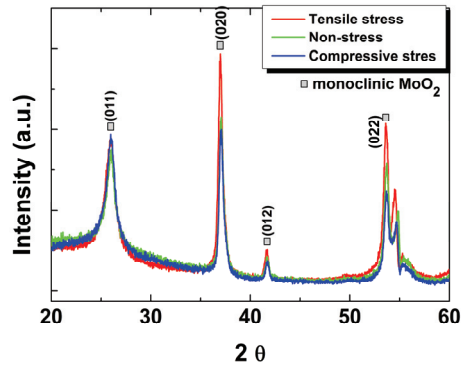
4.1.4. Effects of residual stresses of MoO_x films on crystallization

The author suggested that high compressive stress in the as-deposited ULPS MoO_x films may act as the driving force to promote their crystallization at section 4.1.2. Thus in this section, crystallization behaviors according to the stress conditions of as-deposited MoO_x films were investigated more intensely.

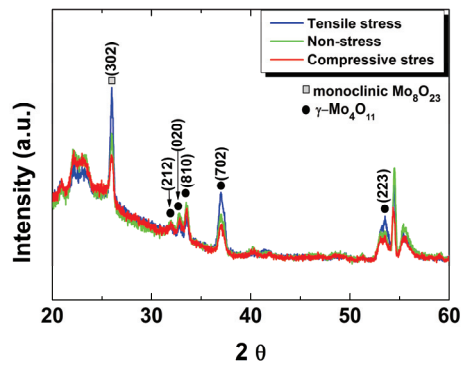
The X-ray diffraction spectra of the films post-deposition annealed (450 °C, 8h, Ar ambient) at different stress conditions are shown in Figure 4.9(a)-(c). The sputtering pressure during deposition was 1.3×10^{-1} Pa in common, and the O/Mo atomic ratios of 2.0, 2.85, and 3.0 were formed at the O₂ contents of 20 %, 30 %, and 40%, respectively. First, in MoO_x films corresponding to O/Mo \approx 2.0 (Fig. 4.9(a)), monoclinic MoO₂ phase only exists in film regardless of stress condition. As the stress applied to the film changes from tensile to compressive, all the MoO₂ peaks become strong and sharp, indicating the grain growth of MoO₂ and an improvement of its crystallinity. In Fig. 4.9(b), monoclinic Mo₈O₂₃ and γ -Mo₄O₁₁, that is, Magnéli phases, are detected, but the correlation between stress and dominant crystal phases is not shown obviously. For the films corresponding to O/Mo \approx 3.0 (Fig. 4.9(c)), the peaks for meta-stable monoclinic MoO₃ only are detected in MoO_x films annealed under tensile stress and non-stress and the XRD patterns for tensile stress and non-stress are nearly identical with each other. While in MoO_x film annealed under compressive stress, monoclinic and orthorhombic peaks of

MoO₃ are mixed. But the intensity of monoclinic MoO₃ peaks sharply decreases with the appearance of typical (0*k*0) orthorhombic MoO₃ peaks.

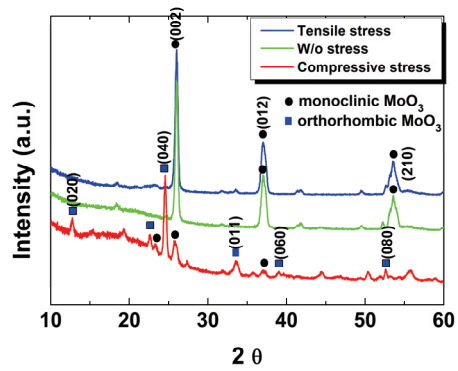
As a result, it can be said that the films annealed under compressive stress with stoichiometric compositions such as O/Mo \approx 2.0 and 3.0 are improved in crystallinity or crystallized to the most stable crystal phase; the former is for the O/Mo atomic ratio of 2.0, and the latter for that of 3.0. This crystallization behaviors may be attributed to the microstructure rearrangement in order to release the compressive stress applied to film. That is, internal strain energy of films will be minimum by crystallizing from amorphous to most stable phase under compressive stress.



(a)



(b)



(c)

Fig. 4.9. XRD patterns of MoO_x films annealed at different stress conditions for $\text{O}/\text{Mo} \approx$ (a) 2.0, (b) 2.85, and (c) 3.0.

4.1.5. Summary

In this chapter, MoO_x thin films have been prepared by the reactive DC magnetron sputtering method on glass and Si/SiO₂ substrates at room temperature. In order to crystallize the films, post deposition annealing was carried out in Ar ambient at 450 °C for 8 hours. The enhanced crystallinity of the films had the effect of elevating the electrical conductivity. It was observed that the resistivity of the films monotonically increased with increasing O₂ content at a sputtering pressure 6.7 x 10⁻¹ Pa, while in the case of those deposited at 1.3 x 10⁻¹ and 6.7 x 10⁻² Pa, there was a local region in which the resistivity decreased with increasing O₂ content. These resistivity variations at low sputtering pressures appeared to be associated with the formation of the monoclinic MoO₂ polycrystalline phase in the films. The MoO_x films exhibiting the minimum resistivity at each sputtering pressure contained only the monoclinic MoO₂ crystalline phase in the amorphous matrix. As the sputtering pressure decreased, the MoO₂ peak intensity in XRD patterns became stronger, resulting in the lowest resistivity value being observed at the lowest sputtering pressure of 6.7 x 10⁻² Pa. This intensive formation of MoO₂ phase at lower sputtering pressures was related to the higher compressive stress of the MoO_x film. Films with high density are usually under high compressive stress and, thus, stress induced crystallization can occur. A very low resistivity was also obtained even at high O₂ contents

such as 40 % O₂ (O/Mo \approx 2.85), in which only monoclinic crystal phases, such as MoO₂, Magnéli, and β -MoO₃, without any orthorhombic MoO₃ phase, were detected in the XRD data. This means that the ULPS MoO_x film formed at the lowest sputtering pressure of 6.7×10^{-2} Pa possessed transparent and conductive properties. Meanwhile through the study for artificial stress test, it was obtained that the films annealed under compressive stress with stoichiometric compositions such as O/Mo \approx 2.0 and 3.0 are improved in crystallinity or crystallized to the most stable crystal phase.

The maximum value of the transmittance was about 73 % within the 400-500 nm wavelength range and the resistivity was 1.05×10^{-3} Ω ·cm in the case of an O₂ content of 40 %. This performance is superior to that of PLD MoO_x films.

4.2. Effects of post-deposition annealing (PDA) temperature on the structural, electrical and optical properties of MoO_x ($x \approx 3$) films

4.2.1. Structural evolution according to PDA temperature

Figure 4.10 shows the XRD patterns of the MoO_x ($x \approx 3$) films annealed at different temperatures. Each film was maintained at its respective temperature for 2 hours in Ar ambient in a vacuum furnace. As shown in Fig. 4.10, the XRD pattern of as-deposited MoO_x film is characteristic for amorphous film. On increasing the annealing temperature the films exhibit polycrystalline nature. For the films annealed from 250 °C to 350 °C, the diffraction peaks corresponding to monoclinic MoO_3 (β -phase) only were detected. In particular, β - MoO_3 (011) and (200) peaks at 23.0° and 25.0°, respectively, were developed with increasing of PDA temperature, while β - MoO_3 (021) peak become small and broad gradually with temperature. Thereafter for the film annealed at 400 °C, typical (0k0) orthorhombic MoO_3 (α -phase) peaks were intensively detected. The same phase transition phenomenon as above can be found in several literatures, which have been suggested that the β -phase converts to the α -phase at temperatures more than 400 °C [121,122]. However unusual phase transformation was exhibited in the MoO_3 film annealed at 450 °C. That is, orthorhombic α - MoO_3 peaks were completely disappeared with

the appearance of three peaks at 22.4°, 33.5°, and 37.2°. They all were identified as γ -Mo₄O₁₁ (Magnéli phase) with orthorhombic symmetry [45,55,56,123]. These phases detected at 450 °C are known to be metallic.

Figure 4.11(a)-(c) show high-resolution TEM images of PDA temperature 350 °C, 400 °C, and 450 °C, respectively, which all show high crystallinity and large grain size.

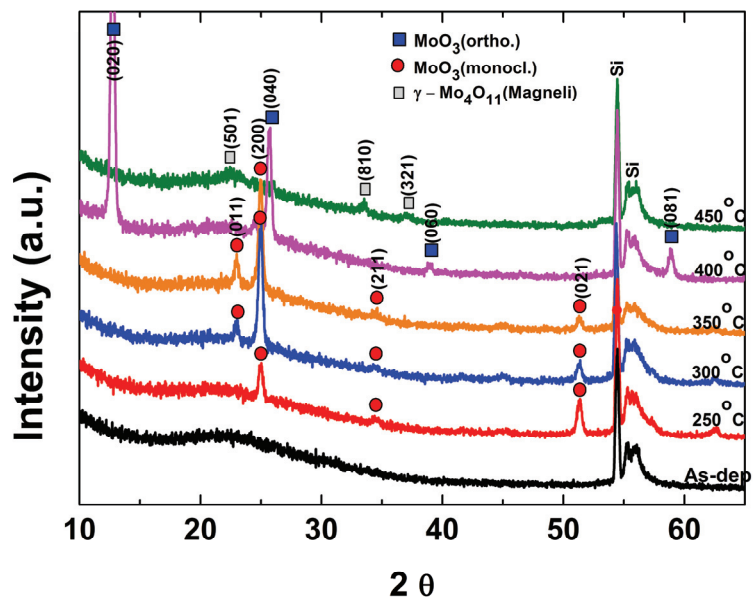
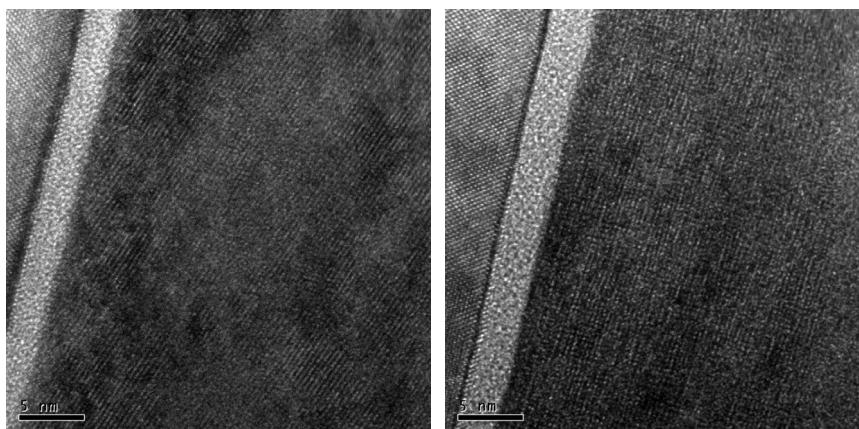
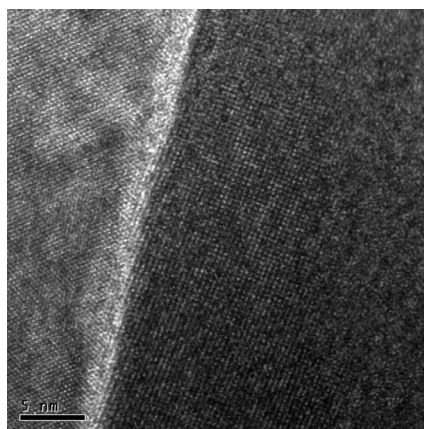


Fig. 4.10. XRD spectra for MoO_x ($x \approx 3$) films with different post-deposition annealing temperature.



(a)

(b)



(c)

Fig. 4.11. Cross-sectional high-resolution TEM images for the PDA temperatures of (a) 350 °C , (b) 400 °C, and (c) 450 °C.

4.2.2. Sublimation behavior and chemical bonding changes

Figure 4.12 shows the change in thickness of MoO_x films measured by ellipsometry, as PDA temperature increases. Initial film thickness was 60 nm and gradual reduction in thickness was observed with increase of temperature. However, the film thickness was rapidly diminished above 400 °C. This film shrinkage behavior is well consistent with the AES measurements, as shown in Fig. 4.13. AES depth profile measurements for oxygen atom were performed by using the sample of $\text{MoO}_x/\text{SiO}_2(100\text{nm})/\text{Si}$ stacks. The two dotted line (1) and (2) in Fig. 4.13 indicate the sharp interface between MoO_x and SiO_2 layer. Only 450 °C PDA film had $\text{MoO}_x/\text{SiO}_2$ interface at the location of line (1), and the films with PDA temperatures less than 400 °C at line (2), indicating thinner MoO_x film in 450 °C PDA.

Figure 4.14(a)-(d) show the cross-sectional SEM images of $\text{MoO}_x(200\text{nm})/\text{SiO}_2(100\text{nm})/\text{Si}$ stacks as a function of PDA condition, that is, 350 °C-2hrs, 400 °C-2hrs, 450 °C-2hrs, and 450 °C-8hrs. These also follow the similar trends of the ellipsometry and AES results. MoO_x films annealed at 350 °C and 400 °C for 2h hrs possessed nearly the same film thickness of 196~198 nm. While, the thickness for the film of 450 °C-2hrs was 183 nm, and longer annealing time (8hrs) resulted in 149 nm-thick film. This means that an annealing of MoO_x ($x \approx 3$) films at 450 °C in Ar gas ambient and under vacuum cause a thinning of film, indicating sublimation of specific MoO_x species.

According to the literature, molybdenum dioxide (MoO_2) is thermally stable up to temperatures above $1000\text{ }^\circ\text{C}$, however in contrast, molybdenum trioxide (MoO_3) tends to sublime below its melting point of $795\text{ }^\circ\text{C}$. Moreover sublimation rates depend on temperature, surface area of the sample, internal geometry of the thermobalance, and gas flow rate [124]. In annealing condition (Ar gas flow rate 200sccm, ambient pressure 10 mTorr) applied in this work, a sublimation of MoO_3 species can be predictable. Furthermore sublimation temperature can be also calculated by using Clausius-Clapeyron equation [125]. Clausius-Clapeyron eq. for equilibrium between a vapor phase and a condensed phase is given by Eq. 4.1 by

$$\ln P = -\frac{\Delta H}{RT} + C \text{ ----- (Eq. 4.1)}$$

where P and T is the pressure and the temperature (K), respectively, and ΔH is the enthalpy of vaporization of solid MoO_3 which value is 740 kJoules [126]. R is gas constant (8.3144 joules/degree·mole) and C is constant. Eq. 4.1 shows that the saturated vapor pressure exerted by a condensed phase increases exponentially with increasing temperature. Minimum temperature vaporized in vacuum of 10 mTorr was estimated to $392\text{ }^\circ\text{C}$, which is well consistent with the ellipsometry and SEM measurement results. Consequently, it is considered that the sublimation of the highest oxygen content species, MoO_3 , at $450\text{ }^\circ\text{C}$ results in oxygen deficiency near the film surfaces and thus

sub-stoichiometric Magnéli MoO_{3-x} ($\gamma\text{-Mo}_4\text{O}_{11}$) phase. In addition, non-oxidizing atmosphere by Ar gas inflow seems to intensify an escape of oxygen ions from the MoO_x ($x \approx 3$) film at high temperatures. A report similar to this result was suggested by Julien *et al* [127]. They reported that vacuum annealed stoichiometric MoO_3 films exhibited a smaller O/Mo ratio, which induced an increasing conductivity. That is, these samples were sub-stoichiometric and possessed more oxygen vacancies in their structure.

Figure 4.15(a) and (b) illustrate the XPS curve-fitting of Mo $3d$ and O $1s$ core level spectra, respectively, of the MoO_x films annealed at temperature of 350 °C, 400 °C, and 450 °C. In Fig. 4.15a, the XP Mo $3d_{5/2, 3/2}$ spin-doublets of Mo^{5+} and Mo^{6+} are shown. The fitted peaks of 231.7 eV and 232.7 eV [128] are assigned to Mo $3d_{5/2}$ of Mo^{5+} and Mo^{6+} , respectively, and Mo $3d_{3/2}$ of two Mo ions are located in the higher binding energy of 3.3 eV. In Fig. 4.15b, each O $1s$ spectra possesses three different peaks consisting of lattice oxygen peak ($\sim 530.2 \pm 0.1$ eV), oxygen vacancy peak ($\sim 530.9 \pm 0.1$ eV), and metal hydroxide peak (OH^-) ($\sim 532.1 \pm 0.1$ eV) [129-131]. Area fractions of Mo^{6+} , Mo^{5+} peaks and three major oxygen-related peaks in MoO_x films produced at PDA temperatures of 350 °C, 400 °C, and 450 °C were summarized in Table 4-2. In particular, 450 °C PDA film among those exhibited unusual increase of Mo^{5+} ion and OH^- species. When a metal combines with oxygen to become a compound, its inner-shell electron binding energy increases slightly [88,132]. Therefore, inversely, the increase of low oxidation state of Mo (Mo^{5+}) with

lower binding energy means escape of slight oxygen atoms from initial film.

A drastic increase of OH^\cdot species seems to be closely related to the sublimation of MoO_3 species and the formation of a lot of oxygen vacancies.

Hydroxyl radicals (OH^\cdot) are very reactive, thus oxygen vacancies and/or broken bonding sites are easily bonded with them.

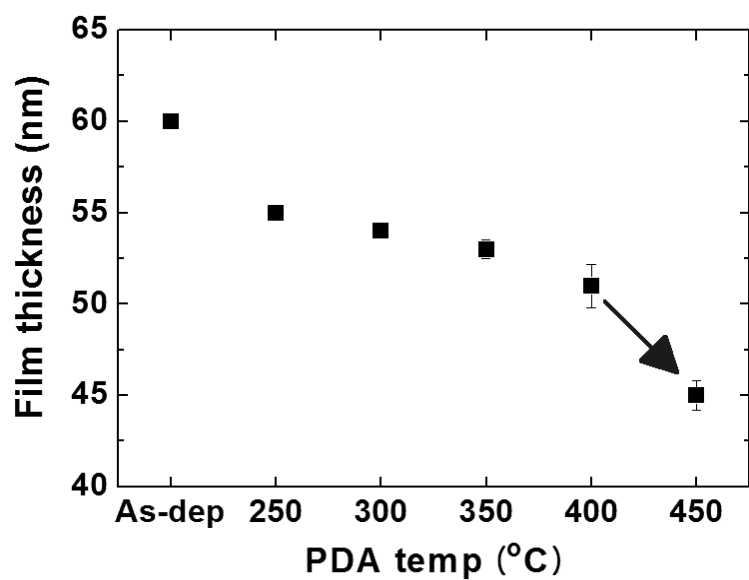


Fig. 4.12. The variation in thickness of MoO_x ($x \approx 3$) films according to post-deposition annealing temperature measured by ellipsometry.

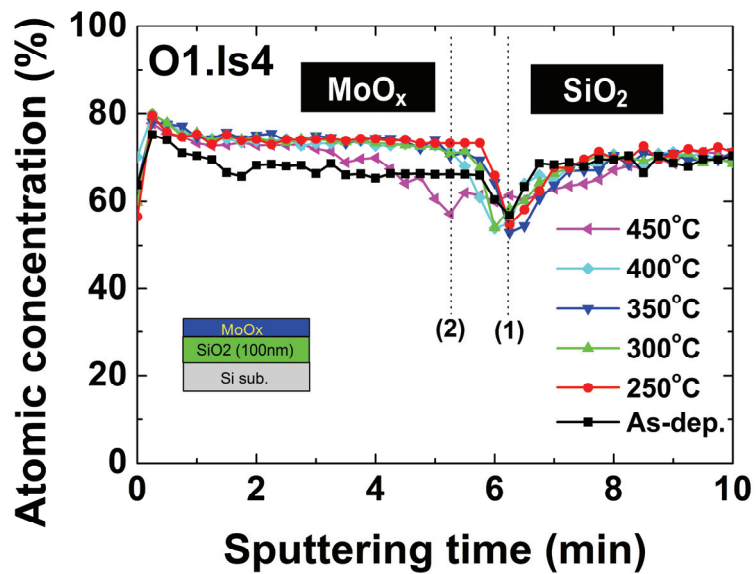


Fig. 4.13. AES depth profiles of MoO_x/SiO₂ (100nm)/Si stacks. The dotted lines (1) and (2) indicate the interface between MoO_x and SiO₂.

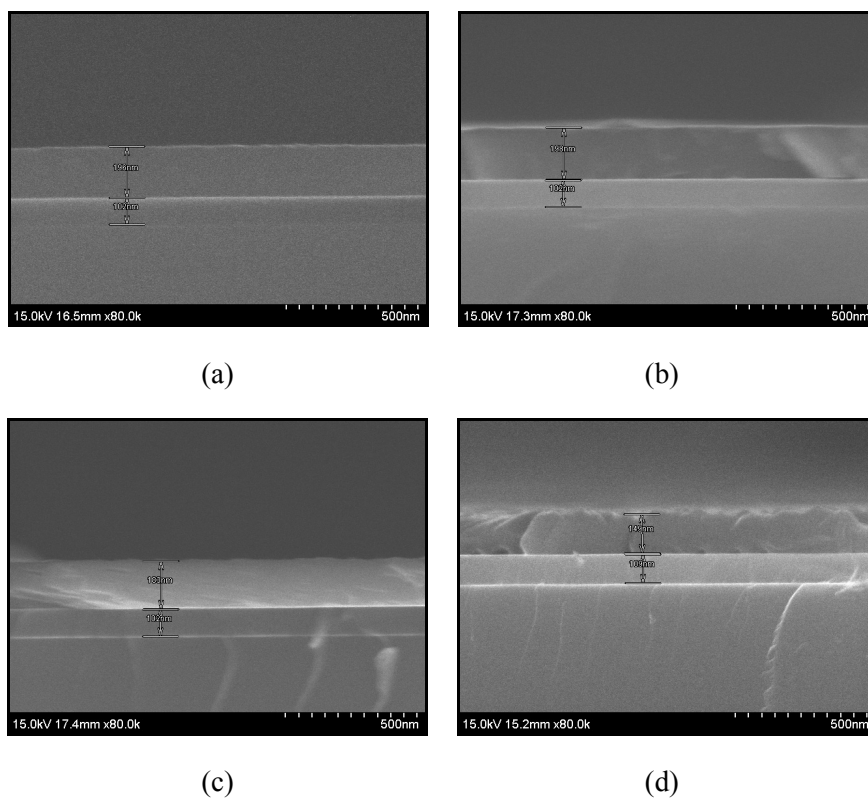


Fig. 4.14. The cross-sectional SEM images of MoO_x/SiO₂(100nm)/Si stacks as a function of post-deposition annealing condition; (a) 350 °C-2hrs, (b) 400 °C-2hrs, (c) 450 °C-2hrs, and (d) 450 °C-8hrs. The thickness of top MoO_x film decreases in proportion to increase of PDA temperature and during-time.

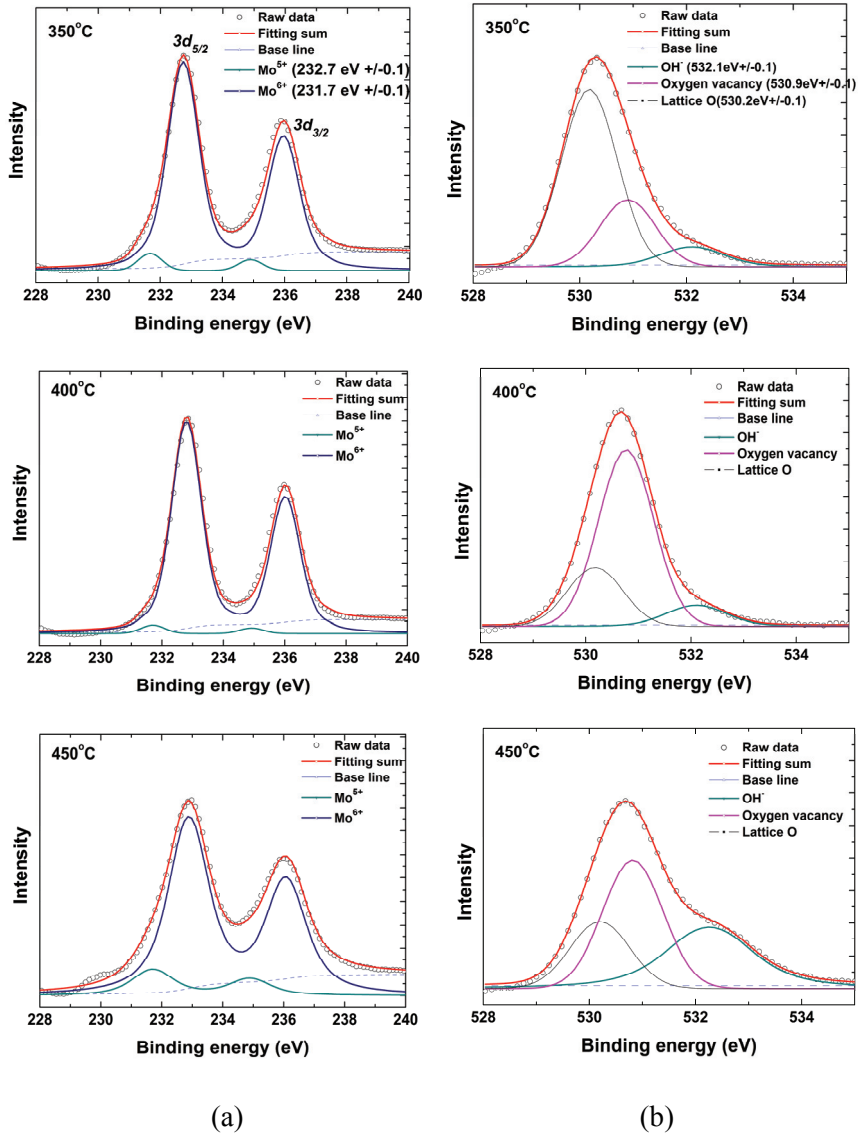


Fig. 4.15. (a) Mo 3d and (b) O 1s XPS spectra of the MoO_x films annealed at temperature of 350 °C, 400 °C, and 450 °C.

Table 4-2. Area fraction of Mo⁶⁺, Mo⁵⁺ and oxygen related peaks in MoO_x films produced at PDA temperatures of 350 °C, 400 °C, and 450 °C.

	350 °C	400 °C	450 °C
Oxygen lattice	66.1	22.6	22.3
Oxygen vacancy	24.8	68.1	43.2
OH ⁻	9.1	9.3	34.5
Mo ⁶⁺	95.1	97.5	87.0
Mo ⁵⁺	4.9	2.5	13.0

$$\ast \text{ Area fraction of } x \text{ species (\%)} = \frac{\text{Area}_x}{\text{Area}_{total}} \times 100$$

4.2.3. Crystalline shapes and surface morphology

Nomarski (or DIC) optical surface micrographs of the MoO_x films with different PDA temperatures are shown in Fig. 4.16(a)-(f). Nomarski images can be seen in striking color (optical contrast) with a 3-dimensional shadowed-like appearance and at excellent resolution [133,134]. Unlike as-deposited film did not have any patterns in its film, MoO_x films annealed from 250 °C to 350 °C possessed needle-shaped crystals with random orientation, of which the areal density increased with the temperature. Particularly, for the film of 250 °C imperfect spherulites having spherical semi-crystalline structure [135] were observed. Hereafter, MoO_x film annealed at 400 °C showed totally different crystal shape, that is, mosaic structure composed of MoO_x grains with different orientation. It can be analogized from XRD result in Fig. 4.10 that each grain is for α -orthorhombic MoO₃. Through further annealing up to 450 °C, sharp and rough, and random-shaped flakes were observed in film surface.

The AFM images in Fig. 4.17(a)-(f) illustrate the surface morphology of the same films with those shown in Fig. 4.16. Table 4-3 summarizes the surface roughness data in terms of root-mean-square roughness (R_{RMS}) and peak to valley roughness (R_{PIV}). Both R_{RMS} and R_{PIV} were exhibited in a similar low level for the films of from 300 °C to 400 °C, while roughness values for 450 °C were considerably large, which seems to be related to the random

sublimation of MoO₃ species in the film surface. Also this result is well corresponded to the XPS result in previous section, in which OH⁻ species sharply increased through 450 °C PDA. Therefore large roughness resulted in large surface area and consequently huge absorptions of OH⁻ species on the surface of film.

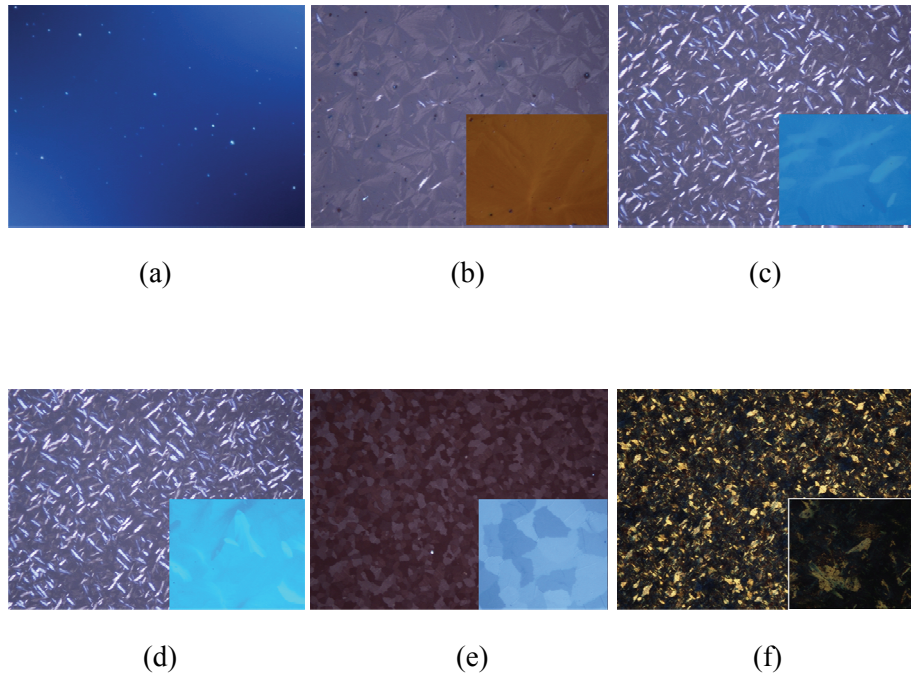


Fig. 4.16. The Nomarski (or DIC) optical surface micrographs of the MoO_x films for magnification of $\times 1000$. (a) as-deposited, (b) 250 °C, (c) 300 °C, (d) 350 °C, (e) 400 °C, and (f) 450 °C annealed films. The inset figure is for magnification of $\times 200$.

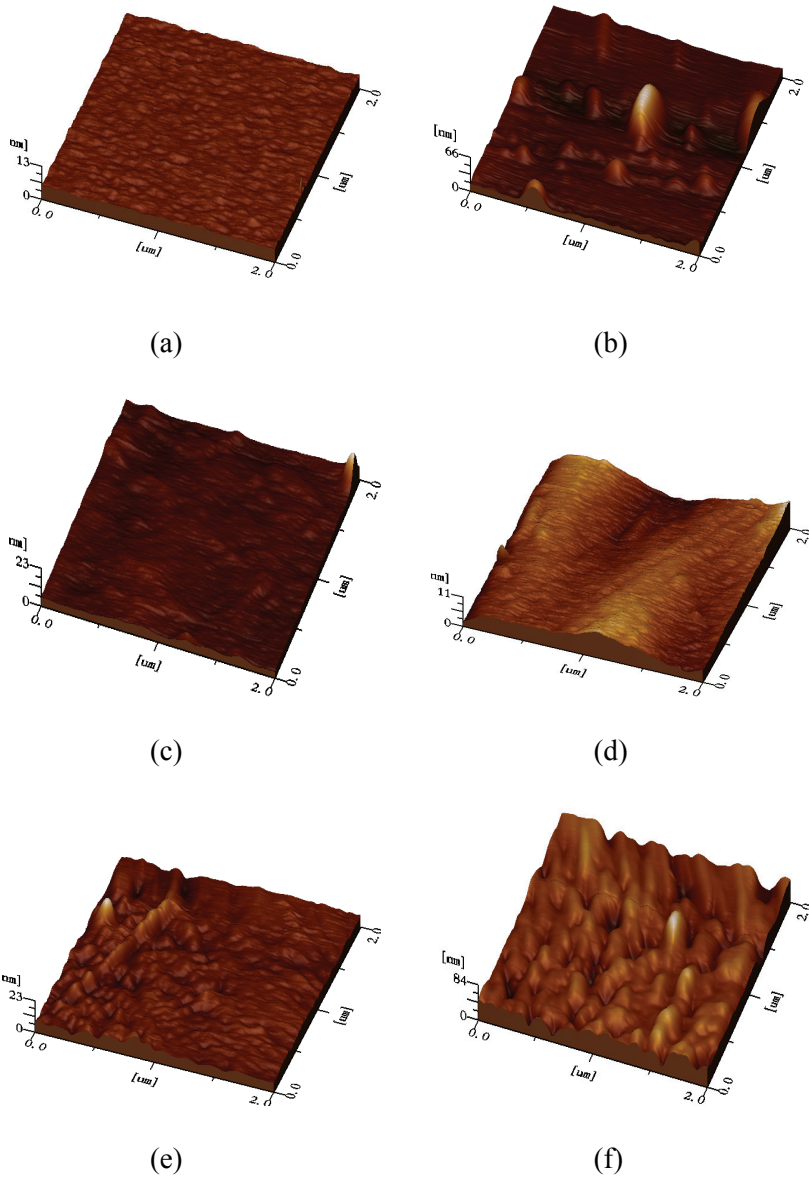


Fig. 4.17. The AFM images of each film: (a) as-deposited, (b) 250 °C, (c) 300 °C, (d) 350 °C, (e) 400 °C, and (f) 450 °C annealed films.

Table 4-3. Comparison of surface roughness of the MoO_x films annealed in different temperature.

PDA temperature (°C)	R_{RMS}	R_{PIV}
As-deposited	0.35 ~ 0.36nm	2.32 ~ 3.54nm
250	3.22 ~ 7.64nm	10.2 ~ 52.8nm
300	0.62 ~ 1.19nm	5.51 ~ 10.6nm
350	1.28 ~ 1.51nm	5.72 ~ 9.14nm
400	1.06 ~ 1.74nm	7.14 ~ 16.1nm
450	8.41 ~ 10.5nm	36.9 ~ 72.4nm

※ R_{PIV} : peak to valley roughness, R_{RMS} : root-mean-square of surface roughness.

4.2.4. Electrical and optical properties

Figure 4.18 presents the electrical properties (resistivity, Hall mobility, and carrier concentration) of MoO_x films annealed at the temperature of 350 °C, 400 °C, and 450 °C. Measured values for films annealed at lower temperatures than 350 °C and as-deposited one could not be obtained due to their too high sheet resistances. The carrier concentrations of 350 °C and 400 °C PDA films were about mid-10¹⁹ cm⁻³, but as PDA temperature increases up to 450 °C, the carrier concentration of the film rapidly increased, reaching a maximum value of 2.0×10^{22} cm⁻³. In contrast, the Hall mobility was inversely proportional to the carrier concentration. Consequently, the resistivity (ρ) calculated by Eq. 3.3a ($\rho = 1/q\mu n$) increased gradually. In case of 450 °C PDA film, the unusual increase of carrier concentration seems to be attributed to the formation of γ -Mo₄O₁₁ phase with the same structure to the ReO₃ which is well known as a degenerated metallic oxide [136]. Moreover Bhosle *et al.* reported that an increase of conductivity (and thus carrier concentration) in MoO_x film was ascribed to the presence of oxygen vacancies and lower oxidation states of Mo such as Mo⁴⁺ and Mo⁵⁺, which is well consistent with our XPS results with high fraction of Mo⁵⁺ in 450 °C PDA film. Meanwhile, the unusual high values of carrier mobility for 350 °C and 400 °C PDA films seem to be result from little ionized impurity scattering and also little grain boundary scattering; the former is due to small carrier concentration less than

10^{20} cm^{-3} [119], and the latter due to large grains as shown in TEM images of Fig. 4.11(a) and (b). Considering the typical carrier concentrations of TCO of the order of 10^{20} cm^{-3} [2], this level of mid- 10^{19} cm^{-3} is thought to be a little low. Actually in case of 350 °C and 400 °C PDA films, poor Ohmic contact phenomenon occurred frequently.

Figure 4.19(a) and (b) shows the optical transmittance for ITO and MoO_x films as a function of wavelength, and their optical band gap energies, respectively. Optical transmittance for 400 °C PDA film was higher than that for 450 °C film in overall wavelength. Optical band gap for 400 °C and 450 °C PDA films was determined as 3.48 eV and 3.25 eV, respectively, as shown in Fig. 4.19(b), in which also 400 °C PDA film possessed higher value than 450 °C film. This is due to the different electronic band structure between orthorhombic MoO_3 and orthorhombic $\gamma\text{-Mo}_4\text{O}_{11}$ phase. Furthermore the decrease in band gap and the increase k_0 absorption in the near infrared region with temperature is reported to be due to the formation of oxygen vacancies in the films [137]. The transparent conductive oxide (TCO) performance of ITO and MoO_x films were summarized in Table 4-4.

Even if the optical transmittance of MoO_x films is inferior to ITO as a reference film, fine adjusting during film preparation probably enables the MoO_x films to have enhanced TCO performance

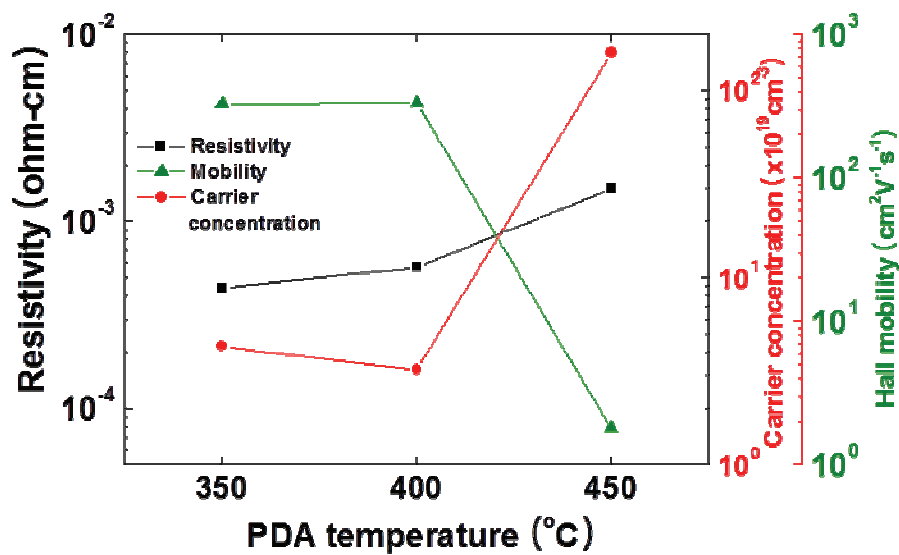
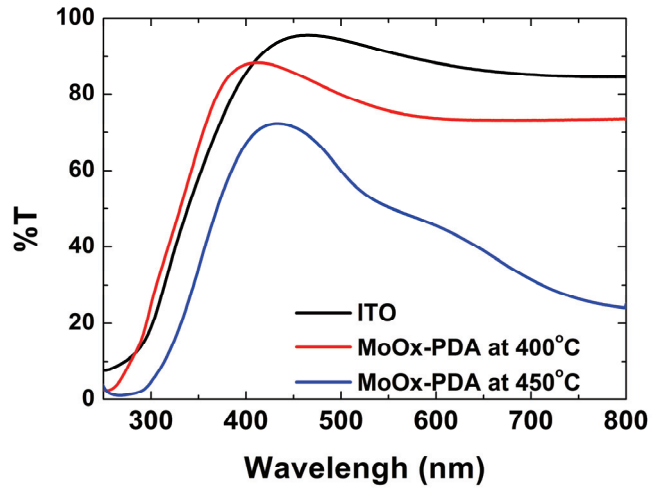
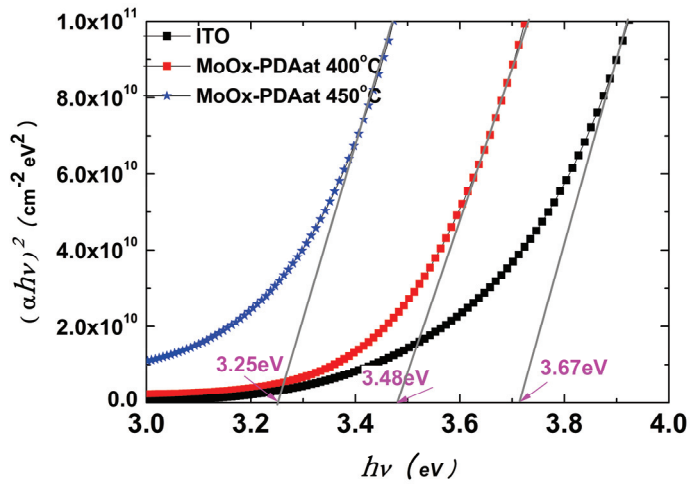


Fig. 4.18. Variation of the electrical resistivity (ρ), Hall mobility (μ), and carrier concentration (n) of MoO_x films annealed at the temperature of 350 °C, 400 °C, and 450 °C.



(a)



(b)

Fig. 4.19. (a) optical transmittance as a function of wavelength and (b) optical band gap energies for ITO and MoO_x films.

Table 4-4. Comparison of the transparent conductive oxide (TCO) performance of ITO and MoO_x films.

	MoO _x			ITO
	350 °C	400 °C	450 °C	350 °C
Resistivity (Ω·cm)	4.4×10 ⁻⁴	5.7×10 ⁻⁴	1.5×10 ⁻³	2.6×10 ⁻³
Mobility (cm ² /V·s)	327	337	2.56	8.05
Carrier concentration (cm ⁻³)	4.3×10 ¹⁹	3.2×10 ¹⁹	1.6×10 ²¹	3.0×10 ²⁰
Transmittance (550nm)	-	76 %	50%	91%
Optical band gap (eV)	-	3.25	3.48	3.67
Figure of Merit (×10 ⁻³ Ω ⁻¹) at max %T	-	3.7	0.24	2.4

4.2.5. Summary

In this chapter, MoO_x ($x \approx 3$) films were annealed at the temperatures of from 250 °C to 450 °C for 2 hours and their structural, electrical, and optical properties were investigated. As-deposited MoO_x film was amorphous, and as the annealing temperature increased the films exhibited polycrystalline nature. The films annealed below 350 °C were crystallized in monoclinic MoO_3 (β -phase), and PDA at 400 °C produced orthorhombic α - MoO_3 phase. Meanwhile, in the MoO_3 film annealed at 450 °C, orthorhombic α - MoO_3 phase was completely disappeared with the appearance of γ - Mo_4O_{11} (Magnéli phase) with orthorhombic symmetry, which phases are known to be metallic.

It was verified that sub-stoichiometric Magnéli MoO_{3-x} (γ - Mo_4O_{11}) phase was formed through 450 °C PDA due to the comparatively intense sublimation of MoO_3 species and loss of oxygen ions in initial film.

The carrier concentrations of 350 °C and 400 °C PDA films were about mid- 10^{19} cm^{-3} , and that of 450 °C PDA films was $1.6 \times 10^{21} \text{ cm}^{-3}$. This unusual increase of carrier concentration with PDA temperature seems to be attributed to the formation of γ - Mo_4O_{11} phase as well as increase of lower oxidation states (Mo^{5+}). In contrast, the Hall mobility was inversely proportional to the carrier concentration. Consequently, the resistivity (calculated by using a term of the product of carrier concentration and

mobility) increased gradually with the PDA temperature. The resistivity values were $4.4 \times 10^{-4} \Omega \cdot \text{cm}$ for 350°C , $5.7 \times 10^{-4} \Omega \cdot \text{cm}$ for 400°C , and $1.5 \times 10^{-3} \Omega \cdot \text{cm}$ for 450°C .

The optical transmittance for 400°C and 450°C PDA MoO_x films was 76 % and 50 % in the wavelength of 550 nm, respectively. The optical band gap energies for 400°C and 450°C PDA MoO_x films were determined as 3.48 eV and 3.25 eV, respectively.

4.3. Preparation and TCO properties of In:MoO_x films

4.3.1. Indium doping effect on crystallization behavior

Figure 4.20 shows the XRD patterns of the indium doped MoO_x films (In:MoO_x) annealed in the range from 250 °C to 450 °C. Indium content in the films was 1.8 at %, obtained by XRF. In a same way to the section 4.2, each film was maintained at its respective temperature for 2 hours in Ar ambient in a vacuum furnace. Compared with XRD patterns for MoO_x ($x \approx 3$) in Fig. 4.10, by and large, crystallization temperature shift to higher temperature was observed. The film annealed at 250 °C still showed amorphous character. Moreover even 400 °C PDA film could not completely transform to the orthorhombic α - MoO₃ phase, which was obtained by 450 °C PDA at last. This hindrance of crystallization for the In:MoO_x films during PDA seems to be due to the large radii of In³⁺ ions. The ionic radii of In³⁺ and Mo⁶⁺ are 0.80 nm and 0.59 nm [138], respectively, indicating larger ionic radius of In³⁺ than Mo⁶⁺. This result is very similar to the report of Choi *et al.*, who described that the crystallization of ITO films was interrupted by adding Yb³⁺ (0.81 nm) and Sm³⁺ (0.91 nm) ions with larger radii into ITO matrix [139].

In addition, sub-stoichiometric Magnéli or hydrogen molybdenum bronze phases shown in MoO_x ($x \approx 3$) film for 450 °C were not detected at all.

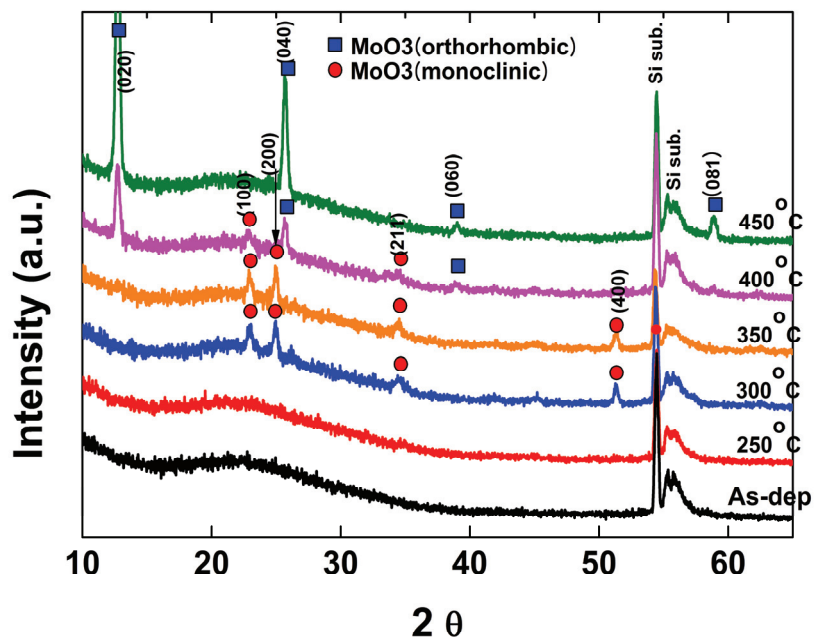


Fig. 4.20. XRD spectra for In:MoO_x (In 1.8 at %) films with different post-deposition annealing temperature.

4.3.2. Influence of Indium doping concentration on electrical and optical properties

The influence of indium doping concentration on electrical properties of In:MoO_x films was investigated. The sputter deposited films with thickness of 100 nm were annealed at the temperature of 400 °C for 2 hours in Ar ambient. The variations of the electrical resistivity, Hall mobility, and carrier concentration of the In:MoO_x films with different indium content were shown in Figure 4.21. By Hall measuring all the In:MoO_x films were identified as p-type.

As the indium content increased, the resistivity gradually decreased until the indium content reached 3.1 at %, and then increased. The resistivity of 3.1 at % In-doped MoO_x film was exhibited in $7.05 \times 10^{-4} \Omega \cdot \text{cm}$. While a variation of hole concentration (n) was inversely proportional to resistivity and Hall mobility (μ) exhibited similar values around $330 \text{ cm}^2 \text{V}^{-1} \cdot \text{s}^{-1}$ for all the films, which value is extremely high. But considering the μ -n relationship calculated using the BHD theory [2] which is based on ionized impurity scattering, these mobility values with hole concentrations of mid- 10^{19} cm^{-3} is reasonable. Up to 3.1 at % indium content, the increase of carrier concentration may be attributed to the effect of substituting Mo⁶⁺ with In³⁺ ions, resulting in generation of 3 holes per one In³⁺. However additional

indium doping seems to be exceed solid solubility of indium in MoO_x film, resulting in precipitation of In atoms or In₂O₃ compounds which can generate electrons.

Figure 4.22(a) and (b) show the optical transmittance (%) and optical band gap energies for In: MoO_x films with different indium content. In Fig. 4.22(a), it was observed that with increasing indium content, that is, hole carrier concentration, the absorption edge shifted towards smaller wavelength (blue-shift), which indicates an increase of optical band gap. Thus, Fig. 4.22(a) and (b) corresponded well to each other. The increase in band gap is normally attributed to the Burstein-Moss effect [140,141] which suggests filling up to the lowest states in the conduction band for n-type TCOs. Considering p-type in the same way with n-type, it can be thought that when the hole concentration exceeds the critical concentration, the highest states in the valence band are filled with hole, leading to the effective widening of E_g. Critical electron concentration for n-type TCOs is known to $\sim 10^{19}$ cm⁻³, and that for p-type is a little lower level $\sim 10^{18}$ cm⁻³, which heavily doped semiconductors exhibit degeneracy. Consequently, the maximum transmittance and optical band gap for 3.1 at % In-doped film was achieved about 80 % and 3.37 eV, respectively.

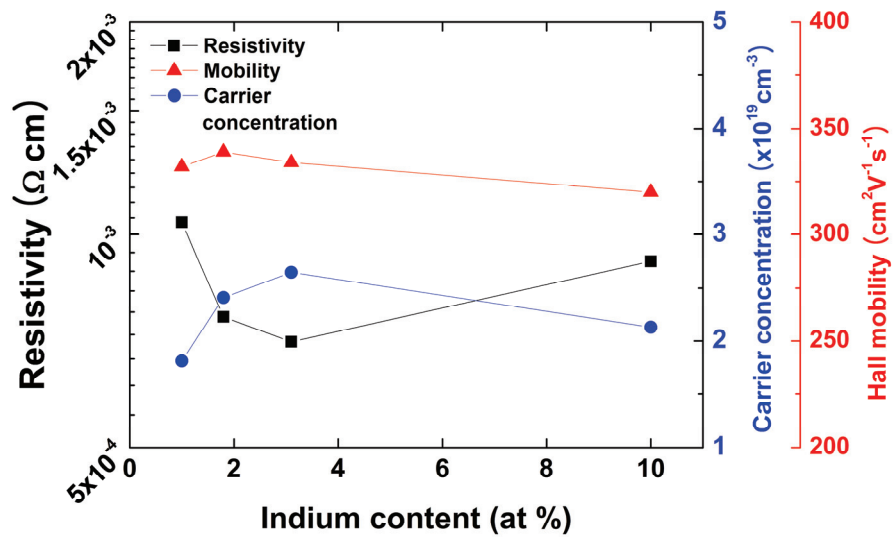
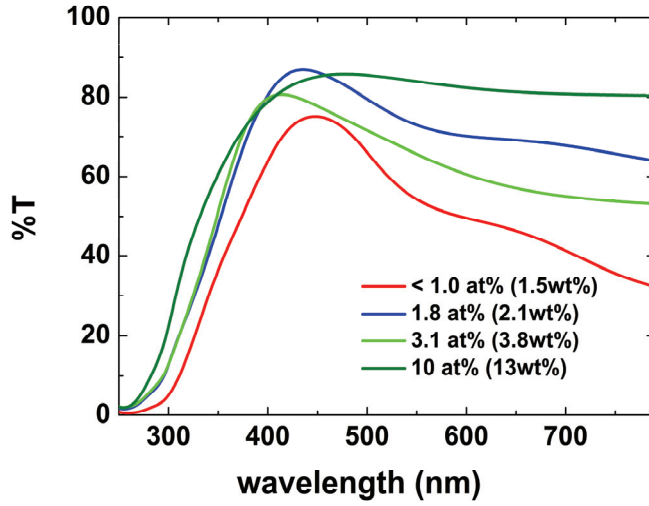
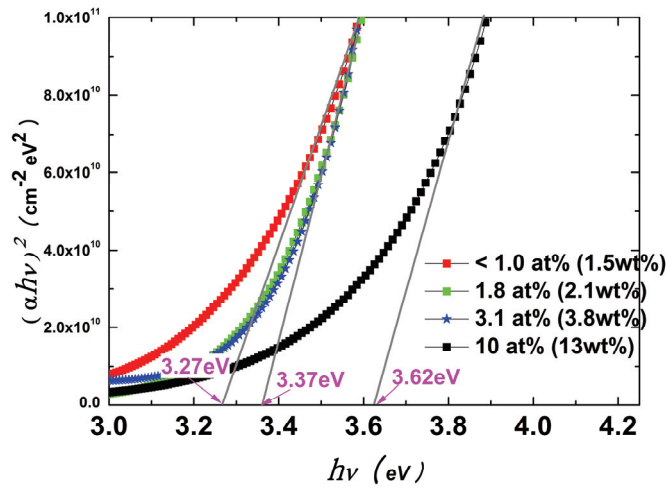


Fig. 4.21. Variation of the electrical resistivity, Hall mobility, and carrier concentration of In:MoO_x films annealed at the temperature of 400 °C for 2 hours, as a function of indium doping concentration.



(a)



(b)

Fig. 4.22. Optical transmittance as a function of wavelength and (b) optical band gap energies for In: MoO_x films with different indium doping concentration.

4.3.3. Summary

In this chapter, indium doped MoO_x (In:MoO_x) films were prepared with MoIn compound target by dc reactive magnetron sputtering method. By Hall measuring In:MoO_x films were identified as p-type oxide. The structural, chemical, electrical, and optical properties of In:MoO_x films were investigated with some parameters.

From XRD analysis of In:MoO_x films annealed in the range from 250 °C to 450 °C, it was revealed that indium dopants acted as an inhibitor to crystallization in In:MoO_x films.

Also the electrical and optical properties of In:MoO_x films with different indium content were investigated. As the indium content increased up to 3.1 at %, the resistivity gradually decreased and the minimum resistivity was exhibited in $7.05 \times 10^{-4} \Omega\cdot\text{cm}$. The transmittance and optical band gap were also increased with increasing indium content and those for 3.1 at % In-doped film was achieved about 80 % and 3.37 eV, respectively.

V. Conclusion

This dissertation presents the preparation and characterization of molybdenum-based binary and ternary oxide films for applications as a transparent conducting electrode. Two types of TCO, molybdenum oxide (MoO_x) and indium doped molybdenum oxide (In:MoO_x), have been deposited by dc magnetron reactive sputtering, followed by post-deposition annealing (PDA) in argon ambient for crystallization.

First, the TCO properties of MoO_x films formed by the ultra-low pressure sputtering (ULPS) method were demonstrated. A very low resistivity was obtained at O/Mo atomic ratio ≈ 2.85 (high O_2 content), in which only metallic crystal phases, such as MoO_2 , Magnéli, and $\beta\text{-MoO}_3$, without any insulating orthorhombic MoO_3 phase, were detected in the XRD data. This means that the MoO_x films formed by ULPS method can possess better transparent and conductive properties than those formed at higher sputtering pressures. The maximum value of the transmittance was about 73 % within the 400-500 nm wavelength range and the resistivity was $1.05 \times 10^{-3} \Omega\cdot\text{cm}$. This performance was superior to the previously reported PLD MoO_x .

Next, MoO_x ($x \approx 3$) films were annealed at the temperatures from 250 °C to 450 °C in order to investigate material properties according to formed MoO_x phases. The films annealed below 350 °C were crystallized in monoclinic

MoO₃ (β -phase), and PDA at 400 °C produced orthorhombic α -MoO₃ phase. Meanwhile, in the MoO₃ film annealed at 450 °C, γ -Mo₄O₁₁ (Magnéli phase) which are known to be metallic was formed without orthorhombic α -MoO₃ phase. It was verified that sub-stoichiometric Magnéli MoO_{3-x} (γ -Mo₄O₁₁) phase was formed through 450 °C PDA due to the comparatively intense sublimation of MoO₃ species and loss of oxygen ions in initial film. The resistivity values were achieved to 5.7×10^{-4} $\Omega \cdot \text{cm}$ for 400 °C, and 1.5×10^{-3} $\Omega \cdot \text{cm}$ for 450 °C. The transmissions of 400 °C and 450 °C PDA MoO_x films were 76 % and 50 %, respectively.

Finally, indium doped MoO_x (In:MoO_x) films were prepared with MoIn compound target. By Hall measuring In:MoO_x films were identified as p-type oxide. From XRD analysis of In:MoO_x films annealed in the range from 250 °C to 450 °C, it was revealed that indium dopants acted as an inhibitor to crystallization in In:MoO_x films. Also the electrical and optical properties of In:MoO_x films with different indium content were investigated. As the indium content increased up to 3.1 at %, the resistivity gradually decreased and the minimum resistivity was achieved in 7.05×10^{-4} $\Omega \cdot \text{cm}$. The transmittance and optical band gap were increased with increasing indium content and those for 3.1 at % In-doped film was achieved about 80 % and 3.37 eV, respectively.

VI. Bibliography

- [1] M. Ohring, *Materials Science of Films*, 2nd ed., Academic Press, San Diego (2002).
- [2] T. Minami, *Semicond. Sci.* **20**, S35 (2005).
- [3] K. Badeker, *Ann. Phys. (Leipzig)*, **22**, 749 (1907).
- [4] A. Hjortsberg, I. Hamberg and C. G. Granqvist, *Thin Solid Films*, **90**, 323 (1982).
- [5] T. Minami, H. Sato, H. Nanto and S. Takata, *Thin Solid Films*, **176**, 277 (1989).
- [6] D. S. Ginley, *Handbook of Transparent Conductors*, p. 524, Springer, New York (2010).
- [7] D. S. Ginley and C. Bright, *MRS Bull* **25**, 15 (2000).
- [8] H. L. Hartnagel, A. L. Dawar, A. K. Jain, and C. Jagadish, *Semiconducting Transparent Thin Films*, p. 1, Institute of Physics Publishing, Bristol and Philadelphia (1995).
- [9] J. L. Vossen, *Phys. Thin Films*, **9**, 1 (1977).
- [10] G. Haake, *Annu. Rev. Mater. Sci.*, **7**, 73 (1977).
- [11] I. Hamberg and C. G. Granqvist, *J. Appl. Phys.*, **60**, R123 (1986).
- [12] J. C. Manifacier, *Thin Solid Films*, **90**, 297 (1982).
- [13] Z. M. Jarzebski, *Phys. Status Solidi A* , **71**, 13 (1982).

- [14] H. Kawazoe, *Nature*, **389**, 939 (1997).
- [15] K. Ueda, T. Hase, H. Yanagi, H. Kawazoe, H. Hosono, H. Ohta, M. Orita and M. Hirano, *J. Appl. Phys*, **89**, 1790 (2001).
- [16] A. Kudo, H. Yanagi, H. Hosono, H. Kawazoe, *Appl. Phys. Lett.*, **73**, 220 (1998).
- [17] E. Bobeico, F. Varsano, C. Minarini and F. Roca, *Thin Solid Films*, **44**, 70 (2003).
- [18] Y. Ogo, H. Hiarmatsu, K. Nomura, H. Yanagi, T. Kamiya, M. Hirano, H. Hosono, *Appl. Phys. Lett.*, **93**, 032113 (2008).
- [19] K. Marsuzaki, K. Nomura, H. Yanagi, T. Kamiya, M. Hirano, H. Hosono, *Appl. Phys. Lett.*, **93**, 202107 (2008).
- [20] W. Shin, N. Murayrama, *Mater. Lett.*, **45**, 302 (2000).
- [21] H. Kawazoe, H. Yanagi, K. Ueda, and H. Hosono, *MRS bulletin*, **25**, 28 (2000).
- [22] A. N. Banerjee, R. Maity and K. K. Chattopadhyay, *Mater. Lett.*, **58**, 10 (2004).
- [23] A. N. Banerjee, S. Kundoo and K. K. Chattopadhyay, *Thin Solid Films*, **440**, 5 (2003).
- [24] E. R. Braithwaite, J. Haber, *Molybdenum: An Outline of its Chemistry and Uses*, p.146, Elsevier, Amsterdam, The Netherlands (1994).
- [25] Claire Schlenker, *Low-Dimensional Electronic Properties of Molybdenum Bronze and Oxides*, Kluwer Academic Publishers, Dordrecht

- (1989).
- [26] V. Bhosle, A. Tiwari, and J. Narayan, *J. Appl. Phys.*, **97**, 083539 (2005).
- [27] J. B. Goodenough, *Chemistry and Uses of Molybdenum*, p.1, Climax Molybdenum Co. (1982).
- [28] J. B. Goodenough, *Bull. Soc. Chim.*, 1200 (1965).
- [29] J. B. Goodenough, *Czech. J. Phys.*, **B17**, 304 (1967).
- [30] P. G. Dickens and K. J. Neild, *Trans. Faraday Soc.*, **64**, 13 (1968).
- [31] G. Sperlich, *Z. Physik*, **250**, 335 (1972).
- [32] V. A. Joffe and I. V. Patrina, *Sov. Phys. Sol. State*, **10**, 639 (1968).
- [33] E. Banks and A. Wold, *Preparative Inorganic reactions*, Vol. **4**, p.237, Interscience (1968).
- [34] P. Hagenmuller, *Progress in Solid State Chemistry*, Vol. **5**, p.71, Pergamon (1971).
- [35] L. Kihlborg, *Arkiv Kemi.*, **21**, 357 (1963).
- [36] E. M. McCarron, *J. Chem. Soc., Chem. Commun.*, **4**, 336 (1986).
- [37] E. Salje, R. Gehlig, *J. Solid State Chem.*, **25**, 239 (1978).
- [38] J. B. Parise, E.M. McCarron, A.W. Sleight, *Mater. Res. Bull.*, **22**, 803 (1987).
- [39] J. B. Parise, E.M. McCarron, R. Von Dreele, J.A. Goldstone, *J. Solid State Chem.*, **93**, 193 (1991).
- [40] A. D. Sayede, T. Amriou, M. Pernisek, B. Khelifa, C. Mathieu, *Chem. Phys.*, **316**, 72 (2005).

- [41] B. G. Bjorn, *Acta Chem. Scand.*, **21**, 661 (1967).
- [42] M. Ghedira, C. Do-Dinh, M. Marezio, and J. Mercier, *J. Solid State Chem.*, **59**, 159 (1985).
- [43] D. B. Rogers, R. D. Shannon, A. W. Sleight, and J. L. Gillson, *Inorg. Chem.*, **8**, 841 (1969).
- [44] A. Magnéli, *Acta Chem. Scand.*, **2**, 501 (1948).
- [45] A. Magnéli, *Acta Chem. Scand.*, **2**, 861 (1948).
- [46] A. Magnéli, *Nova Acta Regiae Soc. Sci. Upsaliensis*, **4**, 14, No. 8 (1950).
- [47] A. Magnéli, B. Blomberg-Hansson, L. Kihlborg, and G. Sundkivist, *Acta Chem. Scand.*, **9**, 1382 (1955).
- [48] G. Hägg and A. Magnéli, *Rev. Pure and Appl. Chem. (Australia)Scand.*, **4**, 235 (1954).
- [49] L. Kihlborg, *Acta Chem. Scand.*, **14**, 1612 (1960).
- [50] L. Kihlborg, *Acta Chem. Scand.*, **17**, 1485 (1963).
- [51] L. Kihlborg, *Arkiv Kemi.*, **21**, 427 (1963).
- [52] L. Kihlborg, *Arkiv Kemi.*, **21**, 443 (1963).
- [53] L. Kihlborg, *Arkiv Kemi.*, **21**, 461 (1963).
- [54] L. Kihlborg, *Arkiv Kemi.*, **21**, 471 (1963).
- [55] L. Kihlborg, *Arkiv Kemi.*, **21**, 365 (1963).
- [56] S. Asbring and L. Kihlborg, *Acta Chem. Scand.*, **18**, 1571 (1964).
- [57] X. Sha, L. Chen, A. C. Cooper, G. P. Pez, and H. Cheng, *J. Phys. Chem. C*, **113**, 11399 (2009).

- [58] R. Rousseau, E. Canadell, P. Alemany, D. H. Galvan, R. Hoffmann, *Inorg. Chem.*, **36**, 4627 (1997).
- [59] M. S. Whittingham, *Solid State Ionics*, **168**, 255 (2004).
- [60] E. Fortunato, D. Ginley, H. Hosono and D. C. Paine, *MRS Bull.*, **32**, 242 (2000).
- [61] G. Gonçalves, E. Elangovan, P. Barquinha, L. Pereira, R. Martins and E. Fortunato, *Thin Solid Films*, **515**, 8562 (2007)
- [62] I. Baía, M. Quintela , L. Mendes, P. Nunes and Martins R, *Thin Solid Films*, **337**, 171 (1999).
- [63] M. F. A. M. Van Hest, M. S. Dabney, J. D. Perkins, D. S. Ginley and M. P. Taylor, *Appl. Phys. Lett.*, **87**, 032111 (2005).
- [64] T. Koida and M. Kondo, *J. Appl. Phys.*, **101**, 063705 (2007).
- [65] Y. Meng, X. Yang, H. Chen, J. Shen , Y. Jiang, Z. Zhang and H. Hua, *Thin Solid Films*, **394**, 219 (2001).
- [66] P. F. Newhouse, C. H. Park, D. A. Keszler, J. Tate and P. S. Nyholm, *Appl. Phys. Lett.*, **87**, 112108 (2005).
- [67] Y. Meng, X. Yang, H. Chen, J. Shen, Y. Jiang, Z. Zhang and Z. Hua, *J. Vac. Sci. Technol. A* **20(1)**, 288 (2002).
- [68] J. E. Medvedeva, *Phys. Rev. Lett.* **97**, 086401 (2006).
- [69] H. Y. Chen, H. C. Su, C. H. Chen, K. L. Liu, C. M. Tsai, S. J. Yen and T. R. Yew, *J. Mater. Chem.*, **21**, 5745 (2011).
- [70] M. F. Al-Kuhaili, S. M. A. Durrani, and E. E. Khawaja, *Thin Solid Films*

- 408**, 188 (2002).
- [71] S. K. Deb and J. A. Chopoorian, *J. Appl. Phys.* **37**, 4818 (1963).
- [72] A. Siokou, G. Leftheriotis, S. Papaefthimiou, and P. Yianoulis, *Surf. Sci.* **294**, 482 (2001).
- [73] M. Yahaya, M. M. Salleh, and I. A. Talib, *Solid-State Ionics* **421**, 113 (1998).
- [74] N. Miyata and S. Akiyoshi, *J. Appl. Phys.* **58**, 1651 (1985).
- [75] J. Scarminio, A. Lourenco, and A. Gorenstein, *Thin Solid Films* **302**, 66 (1997).
- [76] E. Kolawa, C. W. Nieh, F. C. T. So, and M. A. Nicolet, *J. Electron. Mater.* **17**, 425 (1988).
- [77] S. H. Mohamed, O. Kappertz, J. M. Ngaruiya, T. P. Leervad Pedersen, R. Drese, and M. Wuttig, *Thin Solid Films* **429**, 135 (2003).
- [78] K. D. Lee, *Thin Solid Films* **302**, 84 (1997).
- [79] K. Hinojuma, K. Kishimoto and T. Kudo, *J. Electrochem. Soc.* **141**, 876 (1994).
- [80] A. Guerfi and L. A. Dao, *J. Electrochem. Soc.* **136**, 2435 (1989).
- [81] S. Ashraf, C. S. Blackman, G. Hyett, and I. P. Parkin, *J. Mater. Chem.* **16**, 3575 (2006).
- [82] M. S. Huh, B. S. Yang, S. Oh, J. Kim, B. D. Ahn, J. H. Lee, J. Kim, J. K. Jeong, C. S. Hwang, and H. J. Kim, *J. Electrochem. Soc.* **157**, H425 (2009).
- [83] M. S. Huh, B. S. Yang, J. Song, J. Heo, S. J. Won, J. K. Jeong, C. S.

- Hwang, and H. J. Kim, *J. Electrochem. Soc.* **156**, J6 (2009).
- [84] M. S. Huh, B. S. Yang, J. Lee, J. Heo, S. J. Han, K. Yoon, S. H. Yang, C. S. Hwang, and H. J. Kim, *Thin Solid Films* **518**, 1170 (2009)
- [85] H. L. Hartnagel, A. L. Dawar, A. K. Jain, and C. Jagadish, *Semiconducting Transparent Thin Films*, p. 306, Institute of Physics Publishing, Bristol and Philadelphia (1995).
- [86] D. B. Fraser and H. D. Cook, *J. Electrochem. Soc.*, **119** 1368 (1972).
- [87] G. Haacke, *J. Appl. Phys.*, **47** 4086 (1976).
- [88] M. S. Huh, Doctor of Philosophy Dissertation, Seoul National University, Seoul, Korea (2010).
- [89] S. M. Sze, *Physics of Semiconductor Devices*, p. 30, John Wiley & Sons, New York (1981).
- [90] F. M. Smits, *Bell Syst. Tech. J.*, **37**, 711 (1958).
- [91] E. H. Hall, *Am. J. math.*, **2**, 287 (1879)
- [92] L. J. van der Pauw, *Philips Res. Rep.*, **13**, 1 (1958).
- [93] R. A. Smith, *Semiconductors*, 2nd ed., Cambridge University Press, London (1979).
- [94] W. D. Nix, *Metall. Mater. Trans. A*, **20**, 2217 (1989).
- [95] G. C. Stoney, *Proc. Roy. Soc. London*, **A32**, 172 (1909).
- [96] A. J. Griffin, Jr., F.R. Brotzen, and C. Dunn: *Scripta Metall.*, **20**, 1271 (1986).
- [97] M. Ohring, *Materials Science of Films*, 2nd ed., p. 725, Academic Press,

- San Diego (2002).
- [98] V. K. Sabhapathi, O. M. Hussain, P. S. Reddy, K. T. Ramakrishna Reddy, S. Uthanna, B. S. Naidu, and P. Jayarama Reddy, *Phys. Stat. Sol.(a)*, **148**, 167 (1995).
- [99] M. Ohring, *Materials Science of Films*, 2nd ed., Academic Press, San Diego (2002).
- [100] H. F. Winters and E. Kay, *J. Appl. Phys.*, **38**, 3928 (1967).
- [101] R. F. Bunshah, J. M. Blocher, D. M. Mattox, T. D. Bonifield, G. E. McGuire, J. G. Fish, M. Schwartz, P. B. Ghate, J. A. Thornton, B. E. Jacobson, and R. C. Tucker, *Deposition Technologies for Films and Coatings*, Noyes Publications, USA, (1982).
- [102] K. Suzuki and M. Mizuhashi, *Thin Solid Films*, **97**, 119 (1982).
- [103] Y. Wang, J. W. Seok, and R. Y. Lin, *Mater. Res. Soc. Symp. Proc.*, **750**, 307 (2002).
- [104] F. Engelmark, G. Fuentes, I. V. Katardjiev, A. Harsta, U. Smith, and S. Berg, *J. Vac. Sci. Technol. A*, **18**, 1906 (2000).
- [105] B. J. Lee, C. S. Lee, and J. C. Lee, *Acta Mater. Chem.*, **51**, 6233 (2003).
- [106] J. A. Nielsen and D. McMorrow, *Elements of Modern X-Ray Physics*, Wiley, New York (2001).
- [107] D. M. Mattox, *Handbook of Physical Vapor Deposition (PVD) Processing*, Noyes Publications, New Jersey (1998).

- [108] J. W. Park, S. Y. Kwon, S. I. Jun, I. N. Ivanov, J. Cao, J. L. Musfeldt, and P. K. Rack, *Thin Solid Films*, **517**, 3222 (2009).
- [109] J. C. Lou, M. S. Lin, J. I. Chyl, and J. H. Shieh, *Thin Solid Films*, **106**, 163 (1983).
- [110] N. S. Murty, G. K. Bhagavat, and S. R. Jawalekar, *Thin Solid Films*, **92**, 347 (1982).
- [111] N. S. Murty, S. R. Jawalekar, *Thin Solid Films*, **108**, 277 (1983).
- [112] A. De and S. Ray, *J. Phys. D: Appl. Phys.*, **24**, 719 (1991).
- [113] B. Stjerna and C. G. Granqvist, *Solar Energy Mater.*, **20**, 225 (1990).
- [114] B. Stjerna and C. G. Granqvist, *Thin Solid Films*, **193/194**, 704 (1990).
- [115] N. Croitoru, A. Seidman, and K. Yassin, *J. Appl. Phys.*, **57**, 102 (1985).
- [116] N. Croitoru, A. Seidman, and K. Yassin, *J. Appl. Phys.*, **116**, 327 (1984).
- [117] C. G. Choi, K. S. No, W. J. Lee, H. G. Kim, S. O. Jung, W. J. Lee, W. S. Kim, S. J. Kim, and C. Yoon, *Thin Solid Films*, **258**, 274 (1995).
- [118] P. Parreira, J. Valente, G. Lavareda, C. Nunes de Carvalho, A. R. Ramos, E. Alves, P. Brogueira, and A. Amaral, *Physica Status Solidi(a)*, **205**, 1957 (2008).
- [119] B. G. Brandt and A. C. Skapski, *Acta Chem. Scand.* **21**, 661 (1967)
- [120] D. B. Rogers, R. D. Shannon, A. W. Sleight, and J. L. Gillson, *Inorg. Chem.* **8**, 841 (1969).
- [121] P. F. Carcia and e. M. McCarron, *Thin Solid Films*, **155**, 53 (1987).
- [122] W. M . R. Divigalpitiya, R. F. Frindt, and S. R. Morrison, *Thin Solid*

- Films*, **188**, 173 (1990).
- [123] M. Ghedira, H. Vincent, M. Marezio, J. Marcus, and G. Fourcaudot, *J. Solid State Chem.*, **56**, 66 (1986).
- [124] C. M. Earnest, *Compositional analysis by Thermo-gravimetry*, ASTM special technical publication, Baltimore, (1988).
- [125] D. R. Gaskell, *Introduction to the thermodynamics of materials*, p. 161, 5th ed., Taylor & Francis, New York (2008).
- [126] D. V. Ragone, *Thermodynamics of materials*, Jon Wiley & Sons, New York (1995).
- [127] C. Julien, A. Khelifa, O. M. Hussain, and G. A. Nazri, *J. Crystal Growth*, **156**, 235 (1995).
- [128] T. H. Fleisch, G. J. Mains, *J. Chem. Phys.* **76**, 780 (1982).
- [129] L. E. Firment, A. Ferretti, *Surf. Sci.*, **129**, 155(1983).
- [130] T. Ishida, H. Kobayashi, and Y. Nakato, *J. Appl. Phys.* **73**, 4344 (1993).
- [131] S. Major, S. Kumar, M. Bhatnagar, K. L. Chopra, *Appl. Phys. Lett.* **49**, 394. (1986).
- [132] Y. Sato, R. Tokumaru, E. Nishimura, P. -K. Song, and Y. Shigesato, *J. Vac. Sci. Technol. A*, **23** 1167 (2005).
- [133] http://www.jic.ac.uk/microscopy/more/t5_5.htm.
- [134] Y. Leng, *Materials Characterization : Introduction to Microscopic and Spectroscopic Methods*, p.34, John Wiley & Sons (Asia) Pte Ltd, Singapore (2008).

- [135] L. Gránásy, T. Pusztai, G. Tegze, J. A. Warren, and J. F. Douglas, *Phys. Rev. E*, **72**, 011605 (2005).
- [136] C. G. Granqvist, *Mat. Sci. Eng.*, **A168**, 209 (1993).
- [137] J. W. Rabalais, R. J. Colton, and A. M. Guzman, *Chem. Phys. Letters*, **29**, 131 (1974).
- [138] <http://abulafia.mt.ic.ac.uk/shannon/radius.php>.
- [139] S. R. Choi, S. H. Cho, S. I. Kim, Y. M. Kang, H. H. Yoon, K. H. Kim, and P. K. Song, *Jpn. J. Appl. Phys.*, **48**, 05EC04 (2009).
- [140] E. Burstein, *Phys. Rev.*, **93** 632 (1954).
- [141] T. S. Möss, *Proc. Phys. Soc. Lond. Ser. B*, **67** 775 (1954).

List of publications

1. Journal

1.1. International

1. Jeong Hyun Moon, Ho Keun Song, Jeong Hyuk Yim, Han Seok Seo, **Myeong Sook Oh**, Jong Ho Lee, Hyeong Joon Kim, Kuan Yew Cheong, Wook Bahng and Nam Kyun Kim, "Effects of Thermally Oxidized-SiN Gate Oxide on 4H-SiC Substrate", *Electrochemical and Solid-State Letters*, 10 (11) H327-H330 (2007).
2. Dae Hwan Kim, Jong Ho Lee, Jeong Hyun Moon, **Myeong Sook Oh**, Ho Keun Song, Jeong Hyuk Yim, Jae Bin Lee and Hyeong Joon Kim, "Improvement of the reverse characteristics of Ti/4H-SiC Schottky barrier diodes by thermal treatments", *Solid State Phenomena*, 124-126, 105-108 (2007).
3. Bong Seob Yang, Myung Soo Huh, Seungha Oh, Ung Soo Lee, Yoon Jang Kim, **Myeong Sook Oh**, Jae Kyeong Jeong, Cheol Seong Hwang, and Hyeong Joon Kim, "Role of ZrO₂ incorporation in the suppression of negative bias illumination-induced instability in Zn-Sn-O thin film transistors", *Appl. Phys. Lett.* 98, 122110 (2011).
4. **Myeong Sook Oh**, Myung Soo Huh, Bong Seob Yang, Jong Ho Lee, Seong Ha Oh, Ung Soo Lee, Yoon Jang Kim, and Hyeong Joon Kim, "Improvement of electrical and optical properties of molybdenum oxide thin films by ultralow pressure sputtering method", *J. Vac. Sci. Technol. A* 30(3) 031501 (2012).

1.2. Domestic

1. **오명숙**, 이종호, 김대환, 문정현, 임정혁, 이도현, 김형준, "Ni/4H-SiC Field Plate Schottky 다이오드 제작 시 과도식각에 의해 형성된 Nickel_Titanium 이중 금속 Schottky 접합 특성과 공정 개선 연구", *Kor. J. Mater. Res.* 19(1) 28 (2009).

2. Proceedings

2.1. International

1. **Myeong Sook Oh**, Ho Keun Song, Jeong Hyun Moon, Jeong Hyuk Yim, Jong Ho Lee, Han Seok Seo, Yu Jin Choi, and Hyeong Joon Kim, "Fabrication of 4H-SiC Schottky barrier diodes with the epilayer grown by Bis-trimethylsilylmethane precursor", *The 7th International Conference on Power Electronics*, PA36, pp. 229-231 (2007).
2. Ho Keun Song, Jong Ho Lee, **Myeong Sook Oh**, Jeong Hyun Moon, Han Seok Seo, Jeong Hyuk Yim, Sun Young Kwon, Hoon Joo Na, and Hyeong Joon Kim, "Schottky barrier diode fabricated by MOCVD-grown epilayer using bis-trimethylsilylmethane precursor", *Materials Science Forum*, 556-557, pp.113-116 (2008).

2.2. Domestic

1. **Myeong Sook Oh**, Jeong Hyun Moon, Jeong Hyuk Yim, Jong Ho Lee, and Hyeong Joon Kim, "Characteristics of Ni Schottky Barrier Diode with a

- Rating of 900V Having Low Forward Voltage Drop”, *15th Korean Conference on Semiconductors*, 2008, February 21, Pyeong Chang, Korea.
2. **Myeong Sook Oh**, Jeong Hyun Moon, Jeong Hyuk Yim, Jong Ho Lee, and Hyeong Joon Kim, “Characteristics of Ni/4H-SiC Schottky Barrier Diode with homogeneous Schottky Barrier Height by Thermal Treatment”, *16th Korean Conference on Semiconductors*, 2009, February 19, Daejeon, Korea.
 3. Do Hyun Lee, Jeong Hyun Moon, **Myeong Sook Oh**, Jeong Hyuk Yim, Han Seok Seo, and Hyeong Joon Kim, “Comparison of Electrical Characteristics of Ti, Ni SiC Schottky Barrier Diodes with Field Limiting Ring Edge Termination Structure”, *16th Korean Conference on Semiconductors*, 2009, February 19, Daejeon, Korea.
 4. **Myeong Sook Oh**, Myung Soo Huh, Bong Seop Yang, Do Hyun Lee, Jeong Hyun Moon, Seung Ha Oh, and Hyeong Joon Kim, “Fabrication and Characterization of MoO_x/4H-SiC Schottky barrier Diodes”, *17th Korean Conference on Semiconductors*, 2010, February 24-26, Daegu, Korea.

3. Conference

3.1. International

1. Dae Hwan Kim, Jeong Hyun Moon, Ho Keun Song, Jeong Hyuk Yim, Jong Ho Lee, Hoon Joo Na, **Myeong Sook Oh**, and Hyeong Joon Kim, "Effects of interface reaction at metal-semiconductor interface on Electrical properties of 4H-SiC Schottky barrier diodes", *IUMRS-ICA 2006*, September 10-14, Jeju, Korea.
2. Jeong Hyun Moon, Kuan Yew Cheong, Ho Keun Song, Jeong Hyuk Yim, **Myeong Sook Oh**, Jong Ho Lee, Wook Bahng, Nam-Kyun Kim, and Hyeong Joon Kim, “Effect of Nitric-Oxide Post-Oxidation Annealing on

- High-Temperature Oxidized 4H-SiC”, *ICSCRM 2007*, October 14-19, Otsu, Japan.
3. Ho Keun Song, Jong Ho Lee, **Myeong Sook Oh**, Jeong Hyun Moon, Han Seok Seo, Jeong Hyuk Yim, Sun Young Kwon, and Hyeong Joon Kim, “Schottky barrier diode fabricated by MOCVD-grown epilayer using bis-trimethylsilylmethane precursor”, *ICSCRM 2007*, October 14-19, Otsu, Japan.
 4. Jeong Hyuk Yim, Jong Ho Lee, Ho Keun Song, Jeong Hyun Moon, Han Seok Seo, **Myeong Sook Oh**, Jae Bin Lee, and Hyeong Joon Kim, “4H-SiC Planar MESFETs with buried-gates”, *ICSCRM 2007*, October 14-19, Otsu, Japan.
 5. Han Seok Seo, Ho Keun Song, Jeong Hyun Moon, Jeong Hyuk Yim, **Myeong Sook Oh**, Jong Ho Lee, Yu Jin Choi, and Hyeong Joon Kim, “Homoepitaxial growth of 4H-SiC by Hot-wall CVD using BTMSM”, *ICSCRM 2007*, October 14-19, Otsu, Japan.
 6. **Myeong Sook Oh**, Ho Keun Song, Jeong Hyun Moon, Jeong Hyuk Yim, Jong Ho Lee, Yu Jin Choi, and Hyeong Joon Kim, “Fabrication of 4H-SiC Schottky barrier diodes with the epilayer grown by Bis-trimethylsilylmethane precursor”, *The 7th International Conference on Power Electronics (ICPE) 2007*, October 22-26, Daegu, Korea.
 7. **Myeong Sook Oh**, Jeong Hyun Moon, Jeong Hyuk Yim, Do Hyun Lee, and Hyeong Joon Kim, “Simulation and Experimental Characteristics of 4H-SiC Schottky Barrier Diodes with Floating Field Ring Edge Termination”, *Materials Research Society (MRS) Spring Meeting 2009*, April 13-17, San Francisco, USA.
 8. Jeong Hyuk Yim, Jeong Hyun Moon, Han Seok Seo, **Myeong Sook Oh**, Do Hyun Lee, Chang Hyun Kim, and Hyeong Joon Kim, “Short channel effects of 4H-SiC planar MESFETs using ion implantation”, *The 13th*

International Conference on Silicon Carbide and Related Materials (ICSCRM) 2009, October 11-16, Nürnberg, Germany.

9. Do Hyun Lee, Jeong Hyuk Yim, **Myeong Sook Oh**, Han Seok Seo, Chang Hyun Kim, and Hyeong Joon Kim, "1900V 4H-SiC Schottky Barrier Diodes with Field Guard Ring Edge Termination", *International Union of Materials Research Societies- International Conference on Electronic Materials (IUMRS-ICEM) 2010, August 22-27, Seoul, Korea.*
10. **Myeong Sook Oh**, Myung Soo Huh, Bong Seob Yang, Seong Ha Oh, and Hyeong Joon Kim, and Hyeong Joon Kim, "Structural, Electrical, and Optical Properties of Molybdenum Oxides Deposited by Ultra-Low Pressure Sputtering", *The 7th Asian Meeting on Ferroelectricity and 7th Asian Meeting on ElectroCeramics (AMF-AMEC) 2010, June 28-July 1, Jeju, Korea.*
11. **Myeong Sook Oh**, Myung Soo Huh, Bong Seob Yang, Jeong Hyun Moon, Do Hyun Lee, Seung Ha Oh, and Hyeong Joon Kim, "Thermal and Electrical Characteristics of MoO₂/4H-SiC Schottky barrier Diodes", *1st International Conference on Materials for Energy 2010, July 4-8, Karlsruhe, Germany.*
12. **Myeong Sook Oh**, Myung Soo Huh, Bong Seob Yang, Seong Ha Oh, Jeong Hyuk Yim, Do Hyun Lee, Chang Hyun Kim, and Hyeong Joon Kim, "Comparison of MoO_x/4H-SiC Schottky contacts formed by Annealing after Reactive Sputtering and Oxidation Annealing of Molybdenum", *Materials Research Society (MRS) Fall Meeting 2011, November 28-December 2, Boston, USA.*
13. Ung Soo Lee, Bong Seob Yang, **Myeong Sook Oh**, and Hyeong Joon Kim, "Experimental Characteristics of SiO₂ and Al₂O₃-ZrO₂ thin film layer for OLED moisture barrier", *Materials Research Society (MRS) Fall Meeting 2011, November 28-December 2, Boston, USA.*

14. **Myeong Sook Oh** and Hyeong Joon Kim, "Preparation and Characterization of Transparent Conducting Molybdenum Oxide Thin Films", *221st Electro-Chemical Society (ECS) Spring Meeting 2012*, May 6-10, Seattle, USA.

3.2. Domestic

1. Jeong Hyun Moon, **Myeong Sook Oh**, Ho Keun Song, Jeong Hyuk Yim, Jong Ho Lee, Hoon Joo Na, Wook Bahng, Nam Kyun Kim, and Hyeong Joon Kim, "Effect of nitridation in gate oxides grown on (0001) 4H-SiC formed by oxidizing the predeposited Si_xN_y", *Korean Crystallographic Association Spring Meeting 2006*, May 26, Seoul, Korea.
2. Jeong Hyuk Yim, Ho Keun Song, Jeong Hyun Moon, Han Seok Seo, Jong Ho Lee, **Myeong Sook Oh**, Hoon Joo Na, Jae Bin Lee, and Hyeong Joon Kim, "Comparison of 4H-SiC High Purity Semi-insulating Substrates and Vanadium-doped Semi-insulating Substrates", *Korean Crystallographic Association Fall Meeting 2006*, November 24, Incheon, Korea.
3. Jeong Hyuk Yim, Jong Ho Lee, Ho Keun Song, Jeong Hyun Moon, Han Seok Seo, **Myeong Sook Oh**, Jae Bin Lee, and Hyeong Joon Kim, "Dry etching of SiC in inductively coupled SF₆/O₂ Plasma", *Korean Crystallographic Association Fall Meeting 2007*, November 16, Seoul, Korea.
4. Jeong Hyun Moon, Ho Keun Song, Jeong Hyuk Yim, **Myeong Sook Oh**, Jong Ho Lee, Wook Bahng, Nam Kyun Kim, and Hyeong Joon Kim, "Effect of Post-Oxidation Annealing on High-Temperature Grown SiO₂/4H-SiC interface", *Korean Crystallographic Association Fall Meeting 2007*, November 16, Seoul, Korea.
5. Han Seok Seo, Ho Keun Song, Jeong Hyun Moon, Jeong Hyuk Yim, **Myeong Sook Oh**, and Hyeong Joon Kim, "Homoepitaxial growth of 4H-SiC by Hot-Wall CVD using BTMSM", *Korean Crystallographic*

Association Fall Meeting 2007, November 16, Seoul, Korea.

6. **Myeong Sook Oh**, Jeong Hyun Moon, Jeong Hyuk Yim, Jong Ho Lee, Han Seok Seo, and Hyeong Joon Kim, “Electrical Characteristics of High Temperature Post-Annealed 4H-SiC Implanted by Aluminum Ions”, *Korean Crystallographic Association Fall Meeting 2007, November 16, Seoul, Korea.*

7. Jong Ho Lee, Jeong Hyuk Yim, Jeong Hyun Moon, **Myeong Sook Oh**, Ho Keun Song, Jae Bin Lee, and Hyeong Joon Kim, “Fabrication of 4H-SiC Schottky UV Photodiodes”, *Materials Research Society of Korea 2007, may 10-11, Muju, Korea.*

8. **Myeong Sook Oh**, Jeong Hyun Moon, Jeong Hyuk Yim, Yu Jin Choi, Jong Ho Lee, and Hyeong Joon Kim, “4H-SiC에 도핑된 Al 이온의 활성화율 향상을 위한 고온 열처리 효과 연구”, *Materials Research Society of Korea 2007, may 10-11, Muju, Korea.*

9. **Myeong Sook Oh**, Jeong Hyun Moon, Jeong Hyuk Yim, Jong Ho Lee, and Hyeong Joon Kim, “Characteristics of Ni Schottky Barrier Diode with a Rating of 900V Having Low Forward Voltage Drop”, *15th Korean Conference on Semiconductors, 2008, February 21, Pyeong Chang, Korea.*

10. **Myeong Sook Oh**, Jeong Hyun Moon, Jeong Hyuk Yim, Jong Ho Lee, and Hyeong Joon Kim, “Characteristics of Ni/4H-SiC Schottky Barrier Diode with homogeneous Schottky Barrier Height by Thermal Treatment”, *16th Korean Conference on Semiconductors, 2009, February 19, Daejeon, Korea.*

11. Do Hyun Lee, Jeong Hyun Moon, **Myeong Sook Oh**, Jeong Hyuk Yim, Han Seok Seo, and Hyeong Joon Kim, “Comparison of Electrical Characteristics of Ti, Ni SiC Schottky Barrier Diodes with Field Limiting Ring Edge Termination Structure”, *16th Korean Conference on Semiconductors, 2009, February 19, Daejeon, Korea.*

12. **Myeong Sook Oh**, Myung Soo Huh, Bong Seop Yang, Do Hyun Lee, Jeong Hyun Moon, Seung Ha Oh, and Hyeong Joon Kim, “Fabrication and Characterization of MoO_x/4H-SiC Schottky barrier Diodes”, *17th Korean Conference on Semiconductors*, 2010, February 24-26, Daegu, Korea.
13. **Myeong Sook Oh** and Hyeong Joon Kim, “Post-annealing temperature effect on electrical, optical, and structural properties of molybdenum oxide thin films”, *The Korean Society of Semiconductor & Display Equipment Technology (KSDET)*, 2012, May 18, Jeju, Korea.

4. Patents

4.1. Domestic

1. 반도체 소자 제조방법, 문정현, 임정혁, **오명숙**, 이종호, 김형준, 등록일, 2008년 6월 17일, 등록번호 100840702 대한민국.

국문초록

최근 투명전도산화물은 디스플레이 산업에서 그 수요가 매우 크다. 주로 사용되고 있는 투명전극으로서는 ITO가 있으나, 인듐의 높은 가격과 낮은 부존량 때문에 ITO 대체 물질 개발에 큰 관심이 집중되고 있다. MoO_x 는 산소공공의 농도와 non-stoichiometry에 따라 전기적, 광학적 특성을 조절할 수 있는 특성 때문에 ITO 대체 물질로서 연구되고 있다. 한편 기존에 주로 연구되어 온 n-형 투명전도막과 아울러 p-형 산화막 또한 수십 년간 연구가 진행되어 오고 있다. 그러나 n-형에 비하여 낮은 전기전도성과 낮은 투과율을 보임에 따라, 고품질의 p-형 투명전도막 개발은 많은 연구자들에게 주요한 목표가 되고 있다.

본 논문에서는 투명전도막으로서의 몰리브데늄계 산화막을 반응성 DC 스퍼터링으로 증착하였고, 그 특성을 연구하였다. 연구에 사용된 물질은 MoO_x 와 인듐도핑 MoO_x 두 종류의 산화막이었다.

MoO_x 연구에서는, 먼저 반응성 스퍼터 공정 변수 중 공정압력이 후열처리된 박막의 결정화에 미치는 영향을 살펴보고, 그 결과 초저압스퍼터링 (ULPS)에서 결정화 특성이 향상되었음을 확인하였다. 그 원인은 박막에 형성된 압축 응력이 박막의 결정화를 촉진시킨다는 것을 추가 실험을 통해 확인할 수 있었고, $\text{MoO}_{2.85}$ 조성의 박막에서 비저항 $1.05 \times 10^{-3} \Omega \cdot \text{cm}$, 최대투과율 73 % 가량의 값을 얻을 수 있었다.

다음으로, 후열처리 온도에 따른 결정상의 변화를 투명전극 특성과 연계하여 고찰하였다. 높은 산소함량의 MoO_x ($x \approx 3$) 박막을 450°C , 아르곤 분위기에서 후열처리하였을 때 금속성의 $\gamma\text{-Mo}_4\text{O}_{11}$ 상이 생성됨을 확인하였고, 투명전극으로 이용하기에 적합한 높은 캐리어 농도 ($\sim 10^{21} \text{ cm}^{-3}$)와 비저항 값 ($1.5 \times 10^{-3} \Omega\cdot\text{cm}$)을 가졌다. 이는 450°C 에서 절연특성을 가지는 orthorhombic $\alpha\text{-MoO}_3$ 종의 박막 표면에서의 승화와 박막 내 산소 함량이 전반적으로 감소함에 따른 결과로 사료된다. 결과적으로 ITO에는 다소 못 미치는 투명전극 특성을 보였으나, 타 연구그룹의 PLD MoO_x 특성보다 우수한 특성을 가지는 MoO_x 박막을 얻을 수 있었다.

인듐도핑 MoO_x 연구에서는, 후열처리 온도에 따른 결정화도를 MoO_x 계와 비교하였으며, 박막 내 인듐 함량에 따른 캐리어 농도 변화 및 비저항, 그리고 광학적 특성 변화에 대해 고찰하였다. 열처리 온도별로 In:MoO_x 의 결정성을 살펴본 결과, 인듐이 박막의 결정화 온도를 높이는 것이 확인되었다. 이는 In^{3+} 이온의 크기가 Mo^{6+} 보다 큰 것에 기인한 결과라고 사료되었다. 인듐 도핑량 3.1 at %인 In:MoO_x 박막에서 최소 비저항 ($7.05 \times 10^{-4} \Omega\cdot\text{cm}$)이 얻어졌고, 광투과율과 광밴드갭이 각각 80%와 3.37 eV이었다.

주요어 : 투명전도산화물, 몰리브데늄산화물, 인듐몰리브데늄산화물, 초저압스퍼터링, 반응성직류마그네트론스퍼터링, 압축응력유도결정화,

P형투명전도산화물

학번 : 2006-30190

오 명 속